The Meteoritical Society

Meteoritics & Planetary Science 1–26 (2025)
doi: 10.1111/maps.14300

Search for pre-accretionary irradiation effects in Calcium-Aluminum inclusions from the CV3 chondrite Allende

P. GHAZNAVI[1]*, C. BURKHARDT[2], F. L. H. TISSOT[3], and I. LEYA[1]

[1]Space Science and Planetology, Physics Institute, University of Bern, Bern, Switzerland
[2]Max-Planck Institut für Sonnensystemforschung, Göttingen, Germany
[3]Division of Geological and Planetary Sciences, The Isotoparium, Caltech, Pasadena, California, USA

***Correspondence**
I. Leya, Space Science and Planetology, Physics Institute, University of Bern, Sidlerstrasse 5, Bern 3012, Switzerland.
Email: ingo.leya@unibe.ch

(Received 08 December 2023; revision accepted 29 November 2024)

Abstract–Calcium-aluminum-rich inclusions (CAIs) are the first objects that formed in the solar accretion disk and therefore provide valuable insights into the evolution of the early solar system. A long-standing question regarding this earliest formative period relates to the storage of CAIs in the 1–4 Myr time period between their formation and later accretion into chondrite parent bodies. Were the CAIs stored in a pre-existing parent body, or in distant parts of the solar accretion disk? In the latter scenario, CAIs might have been exposed to cosmic rays, either from the galaxy or from the Sun and such pre-accretion irradiation effects might be detectable. We searched for such pre-accretional irradiation effects in 7 fine- and 11 coarse-grained CAIs from the CV 3.6 carbonaceous chondrite Allende. The extracted samples were analyzed for their major chemical composition and all samples were analyzed using μCT techniques. Using physical model calculations, $^{21}Ne_{cos}$ and $(^{22}Ne/^{21}Ne)_{cos}$ production rate ratios were calculated for each CAI by fully considering their individual chemical composition. Measured He, Ne, Ar, and Kr isotope compositions of the CAIs show cosmogenic signals; clear signals for He and Ne isotopes; and detectable signals for some of the Ar and Kr isotopes. In addition, most samples show clear indications for radiogenic ^{4}He and some samples show evidence for radiogenic ^{40}Ar. Higher $^{36}Ar/^{38}Ar$, $^{22}Ne/^{21}Ne$, $^{80}Kr/^{84}Kr$, and $^{82}Kr/^{84}Kr$ ratios together with lower cosmogenic $^{38}Ar_{cos}$ concentrations in fine-grained CAIs compared to coarse-grained CAIs are consistent with more alteration of the former compared to the latter. The CRE ages for the CAIs range between 4.12 ± 0.41 Myr and 6.40 ± 0.63 Myr. Statistical tests indicate that the data are normally distributed with no outliers, indicating that all CAIs share a common irradiation history, likely the irradiation in the Allende meteoroid. The average CRE age of 4.87 ± 0.19 Myr agrees with the nominally accepted CRE age of Allende of ~5.2 Myr. There is no correlation between $^{21}Ne_{cos}$ concentrations and indicators of aqueous alteration like Na and/or U concentrations. The lack of correlation together with the finding of normally distributed modeled CRE ages indicates that either none of the studied CAIs experienced a pre-accretion irradiation before parent body compaction and/or that any pre-accretion irradiation effects have been completely erased during aqueous alteration events. Taking alteration aside, the findings are not in favor of X-wind type models but are more consistent with the idea of CAI outward transport in an expanding disk.

INTRODUCTION

Calcium-aluminum-rich inclusions (CAIs) are a refractory component of chondritic meteorites (chondrites). They contain the first minerals expected to condense (e.g., Ca, Al, Ti, Mg-oxides, and silicates) at temperatures above ~1400 K from a cooling gas of solar composition (Grossmann 1972) and are the oldest dated objects formed in the solar system (Amelin et al., 2010). Some CAIs are surrounded by single or multilayered rims that are of accretionary origin and some are surrounded by high-temperature rims that are firmly attached to the CAIs. It is assumed that CAIs formed within less than ~0.2–0.4 million years (Myr) (e.g., Krot et al., 2009; MacPherson et al., 2012) in multiple transient heating events, that is, evaporation–condensation processes, melting, and crystallization (e.g., Grossman et al., 2000, 2008; Hu et al., 2021; Richter et al., 2002). The heating events occurred (i) in high-temperature nebular regions ($T > 1400$ K), (ii) under low total pressure (10^{-6} to 10^{-3} bar), (iii) in a reduced environment, and (iv) in the presence of ^{16}O-rich gas (e.g., Itoh et al., 2004; Krot et al., 2009). The latter is indicated by the finding that most CAIs from primitive, unmetamorphosed chondrites are uniformly ^{16}O-rich (e.g., Krot et al., 2020). CAIs preserved nucleosynthetic isotopic anomalies in Ca, Ti, Si, Cr, Ni, and other elements, indicating incomplete homogenization in the solar nebula (Dauphas & Schauble, 2016). There is some debate about the location of the CAI formation region, which was either throughout the inner protoplanetary disk (1–4 AU) or in a localized region near the proto-Sun (<0.1 AU). For a detailed discussion, see Krot et al. (2009). Likewise, there is debate about the CAI formation process and among the proposed models are shock wave models and X-wind type models (e.g., Richter et al., 2006). However, no matter the formation region and the formation process, there must have been an effective radial transport of CAIs, given their presence in outer solar system objects such as carbonaceous chondrites and samples from comet 81P/Wild 2 (McKeegan et al., 2006).

The accretion age of chondrite parent bodies and hence the timing of the incorporation of CAIs into these bodies are not directly recorded by any radio-chronometer, but are bracketed by the time of the last melting event of the chondrules contained in a particular chondrite and the precipitation of secondary minerals formed during the parent body's aqueous alteration. Despite some debate about (i) the onset and duration of chondrule formation (e.g., Bollard et al., 2017; Fukuda et al., 2022; Pape et al., 2019), (ii) the consistency of different chronometers (e.g., Desch et al., 2023; Larson et al., 2011), (iii) the extend of resetting of chondrule ages by alteration (e.g., Piralla et al., 2023; Siron et al., 2021), and (iv) the models for linking alteration ages to parent body thermal evolution (e.g., Fujiya et al., 2012), it is well established that chondrite parent bodies accreted in a time interval from ~2 Myr after CAIs and until the dispersal of the gas disk ~4 Myr after CAIs (e.g., Sugiura & Fujiya, 2014). This age gap between the formation of CAIs and the accretion of the chondrite parent bodies requires an explanation for the preservation of CAIs in the disk. There are dynamic arguments that CAI-type objects would be lost into the Sun by gas drag on much shorter time scales (Weidenschilling, 1977). There are, however, possible ways to store CAIs in the disk. First, CAIs could be preserved from falling into the Sun because they were stored in some type of planetesimals and were therefore not affected by gas drag. Later, the hypothetical parent body was disrupted and the thus liberated CAIs could re-accrete with the chondrules and the matrix to later generation planetesimals (e.g., Hutcheon et al., 2009). As discussed by Krot et al. (2009), the planetesimal storage hypothesis is not without problems, because the large amount of ^{26}Al in CAIs would lead to thermal processing if not total differentiation of the planetesimals. Since there is no evidence for significant thermal processing of CAIs before accretion to the chondrite parent body, the planetary storage hypothesis is not very likely. Second, several dynamical nebular processes can counteract gas drag and therefore would allow small objects to stay inside the disk for millions of years and not fall into the Sun. One such model is the X-wind model proposed by Shu et al. (1996), whereby CAIs were launched from the so-called reconnection region near the Sun onto the outer regions of the disk (Figure 1a). However, there are some mineralogical arguments against this model (e.g., Desch, 2007; Krot et al., 2009). Alternative models have been proposed, invoking gravitational torques (Boss, 2008) or turbulent diffusion (Cuzzi et al., 2003) to explain the transport of CAIs outward in the disk. The turbulent diffusion model suffers limitations and requires very special, sometimes unrealistic conditions, for example, the region where CAIs formed would have to be enriched in silicates by a factor $>10^3$ (e.g., Ciesla & Cuzzi, 2006; Krot et al., 2009). In addition, the source of the turbulence remains a matter of debate (e.g., Ciesla, 2007a, 2007b). Elaborating on the turbulent diffusion process, Ciesla (2007a, 2007b) showed that, during the earliest stages of disk evolution, the net inward movement of the collapsing proto-molecular cloud is likely accompanied by outward flows in or around the midplane of a turbulent disk. This combination of outward transport and diffusion close to the midplane and rapid inward transport at higher altitudes leads to the finding that outward transport can be more efficient for larger particles because they stay, due to gravitational

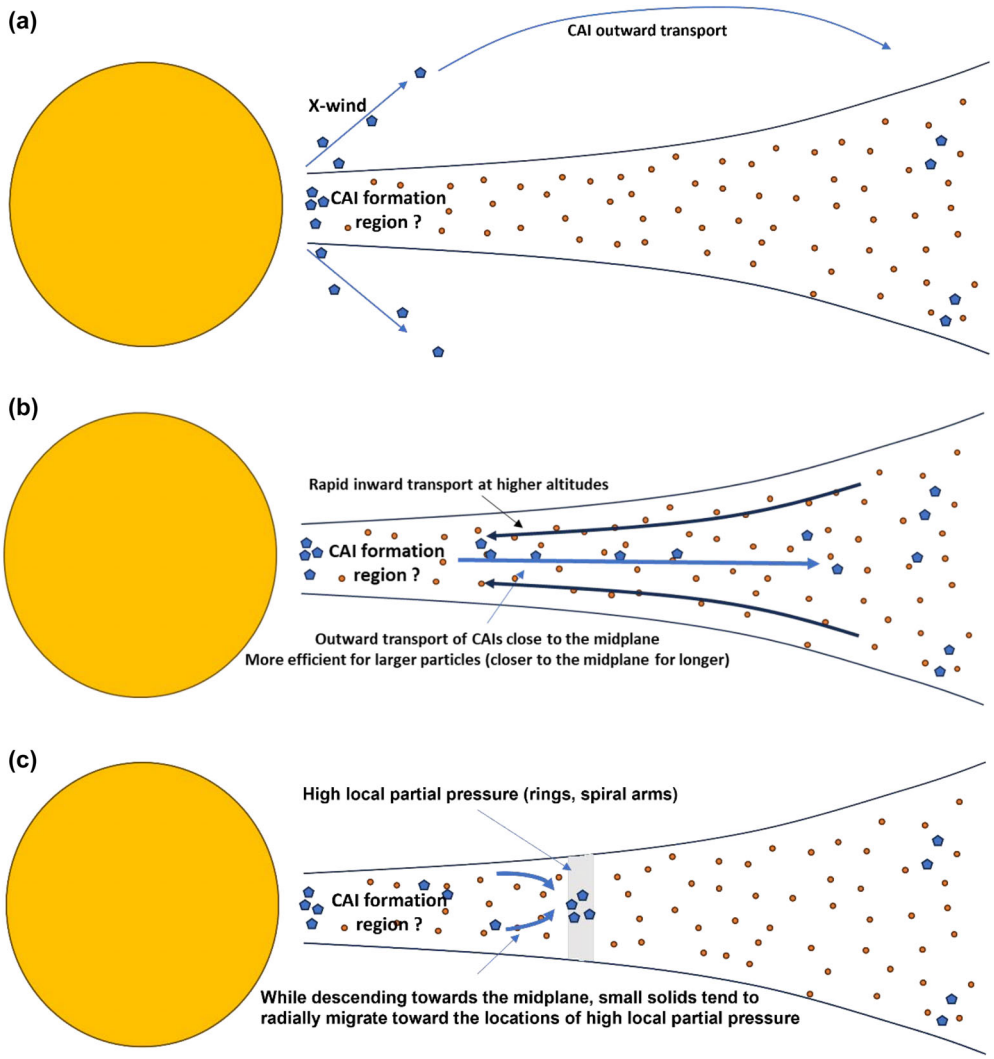

FIGURE 1. Scenarios for CAI formation, transport, and storage in the early solar nebula. (a) X-wind scenario, in which CAIs are likely irradiated by SCR and/or GCR. (b) Outward transport and diffusion in a turbulent solar nebula. CAIs are likely shielded from SCR and GCR because outward transport is close to the midplane. (c) Transport of CAIs to regions of high local pressure and CAI storage in such regions. Depending on the geometry, the region of CAI storage might be accessible to cosmic rays.

settling, close to the midplane for longer time periods (e.g., Ciesla, 2007b, see also Figure 1b). According to the model by Ciesla (2010a, 2011), refractory inclusions that formed early, that is, within the first 10^5 years, have a higher chance of survival until parent body accretion than later formed inclusions because the initial spread of the disk due to transport of angular momentum helps preserving them. Since the largest number of grains is formed in this short period of time, there will be a dominance of early formed refractory inclusions in today's meteorites. Consequently, the short duration of CAI formation as inferred from their ages might simply reflect the higher change of survival for early formed CAIs (e.g., Ciesla, 2010b; Yang & Ciesla, 2012).

Finally, CAIs can be kept in the protoplanetary disk if there are rings and/or spiral arms because small objects would be decoupled from the gas drag and can stay for a long time in the centers of such rings and spiral arms (Haghighipour & Boss, 2003a, 2003b). In essence, while descending toward the midplane, small solids tend to radially migrate toward the locations of high local partial pressure. In this model, small particles spend more time with the gas and therefore take longer to migrate (Haghighipour & Boss, 2003a, 2003b, see also Figure 1c).

The existing dynamical models can be subdivided into two groups. In the first group, CAIs are transported far above the planetary disk (X-wind model) or are stored in rings or spiral arms of high local gas pressure. In such

scenarios, CAIs might be exposed to radiation from solar cosmic rays (SCRs) and/or galactic cosmic rays (GCRs) for long enough to produce measurable cosmogenic nuclide concentrations. Throughout this paper, we refer to such produced cosmogenic nuclides as "excess cosmogenic nuclides." If transport was in the midplane as proposed by, for example, Ciesla (2007a, 2007b), then the CAIs were likely shielded from any type of radiation and no excess cosmogenic nuclides are expected. Consequently, the study of excess cosmogenic nuclides can help to put constraints on possible CAI formation and especially transport mechanisms in the early solar system; was the transport and/or storage in a region accessible to cosmic rays or was it in a region shielded from cosmic rays.

While cosmogenic nuclides in CAIs can put some constraints on CAI formation scenarios, studying excess cosmogenic nuclides is not trivial. Most meteorites acquire the bulk of their cosmogenic nuclides during transit to Earth, that is, in the time after their formation in an asteroid break-up event and before their fall on Earth. Exceptions are regolith breccias, for which parts have been irradiated already on the asteroid parent body. We refer to this part of the irradiation history as "meteorite." Detecting excess cosmogenic nuclides from an irradiation that happened before parent body accretion is challenging. First, because the distribution of (meteorite) cosmogenic nuclides is not uniform but depends on (i) the irradiation time (CRE age), (ii) the pre-atmospheric radius of the meteorite and the pre-atmospheric depth of the sample (both define the shielding depth), and (iii) its chemical composition. Hence, the major challenge in any study of excess cosmogenic nuclides is to prove that detected excesses (if there are any) are real and not simply due to variations in shielding and/or chemical composition. Since excesses are expected to be small, the necessary corrections must be addressed very carefully. Second, there is always a chance that excess signals get lost either during parent body accretion and/or during (aqueous and/or thermal) alteration events on the parent body.

The pioneering study by Vogel et al. (2004) searched for primordial noble gas concentrations in CAIs from the CV3 chondrites Allende, Axtell, and Efremovka. However, since no chemical composition data were measured for the studied CAIs, the authors made no attempt to compare the measured isotope concentrations for the different CAIs and/or to study pre-accretionary irradiation effects.

A recent study found in some peculiar hibonite-rich CAIs from CM chondrites He and Ne excesses, which were attributed to in situ irradiation by energetic particles from the early Sun (Kööp et al., 2018). Since the irradiation signatures were found for noble gases, that is, volatile elements, that are supposed to be lost by diffusion at higher temperatures, the authors inferred that the irradiation happened in a relatively cold region of the disk, that is, at a considerable distance from the Sun. Such high particle fluxes that far out in the solar system would require a highly active early Sun. However, the argument that the spallation produced noble gases would be lost if the irradiation happened in the hotter inner part of the solar system might not be entirely solid. We will show below that it is often difficult to completely degas CAIs even under intense laser heating. Consequently, spallation produced He and Ne isotopes can be relatively robust against diffusion, which might relax the argument that the irradiation must have occurred in the outer colder region of the disk.

We studied He, Ne, Ar, and Kr isotope concentrations in 11 coarse-grained and 7 fine-grained CAIs from the CV 3.6 carbonaceous chondrite Allende. All CAIs were analyzed for their major element composition using μXRF, enabling precise corrections of cosmogenic signatures for variations in chemical composition. In addition, and to prepare for future studies, we established a correlation between cosmogenic ^{21}Ne production rates and the grayscale values (related to the linear attenuation coefficient of X-rays) obtained from μCT data, which enables correction for variations in chemical composition if no measured chemical data exist. Variations in shielding are corrected using new model calculations.

EXPERIMENTAL

Sample Selection

We studied 19 samples from different fragments of the CV 3.6 carbonaceous chondrite Allende. Seventeen of them are typical CAIs. Two of the samples are not typical CAIs; they contain high amounts of Fe and Ni but almost no Ca (Tables 1 and 2). SEM and EDS analyses revealed that sample Test1 is a highly altered CAI, consisting of pyroxene and nepheline. Sample Test2 is an olivine aggregate consisting of olivine, diopside, nepheline, and FeS. These two samples are considered for the rest of the paper only as test samples used to check the procedure. Among the extracted CAIs, 7 are fine-grained (FG) and 11 are coarse-grained (CG). Some of the samples have been studied before. A description of the FG-CAIs can be found in Charlier et al. (2021) (see Table 1 for the alternative names). A detailed description of CG-CAI *Alvin* (a Forsterite bearing type B inclusions, also known as TS−45) is available in Bullock et al. (2012) and MacPherson et al. (2017). The compact type A inclusion *CGft-12* is described in Ma et al. (2022). For other CG-CAIs, which include compact and fluffy type As as well as type B1s and B2s, the inclusion type is listed in Tables 1 and 2.

TABLE 1. Petrologic type of CG-CAIs and alternative names of FG-CAIs from the carbonaceous chondrite Allende (CV3).

Sample	Source	Catalog #	Petrologic type	Other name
Alvin	FM	ME2629-4.109	FoB	
CGft-3	AMNH	4320-CG-1	—	
CGft-5	FM	ME2629-4.72	CTA	
CGft-6	FM	ME2629-4.73	Type B2	
CGft-7	FM	ME2637-2.2	CTA	
CGft-8	FM	ME2639-2.8	Fluffy type A	
CGft-10	FM	ME2639-3.1	Type B1	
CGft-11	FM	ME2639-13.1	Type B1	
CGft-12	FM	ME2639-23.2	CTA	
CGft-13	FM	ME2639-49.6	CTA	
CGft-13Alt				
FGft-12	AMNH	4290-FG-1		Charles[a]
FGft-13	AMNH	4299-FG-1		Erik[a]
FGft-17	AMNH	4321-FG-1		Jean[a]
FGft-19	AMNH	4322-FG-1		Ororo[a]
FGft-23	AMNH	5047-C2/D2-FG-1		Peter[a]
FGft-25	AMNH	5058-FG-1		Raven[a]
FGft-27	AMNH	5064-FG-2		Scott[a]
Test1	FM	ME2629-4.156		
Test2	FM	ME2629-4.157		

Note: The CAIs are distinguished into coarse-grained (CG) and fine-grained (FG). Test1 is a highly altered CAI and Test2 is an olivine aggregate. Both test samples have been used to test the sample handling and noble gas extraction procedures.
Abbreviations: AMNH, American Museum of Natural History (New York); FM, Field Museum (Chicago).
[a]The FG-CAIs have been studied before by Charlier et al. (2021).

For the extraction of CG-CAIs, the Allende samples were cut around the CAIs, and the remaining matrix material was gently removed using SiC abrasive paper. Remaining contamination was removed by handpicking under a binocular microscope based on color and texture differences between CAIs and matrix. This procedure enabled the extraction of CAIs without any remaining matrix contamination. Extraction of FG-CAIs, due to their fragility, required a more delicate approach. The meteorite sample was cut to enable access to the fine-grained inclusions, which were then gently extracted from the meteorite matrix using clean stainless steel dental tools. To minimize matrix contamination, the extracted materials were further inspected under a binocular microscope, and only matrix-free CAI parts (based on differences in color and texture between CAIs and matrix) were taken. After extraction and careful visual inspection, CAIs (both FG and CG) were crushed in an agate mortar dedicated to meteorites. After each sample, the agate mortar was cleaned by grinding high-purity silica and rinsing with ethanol and milliQ-water to avoid cross-contamination. After crushing and homogenization, an aliquot of the CAI powder was taken for the present study, ranging in mass from 8 to 15 mg.

μXRF Measurements

The powdered samples were analyzed for their major chemical composition using μXRF (micro X-ray fluorescence, Bruker Tornado M4 with Rh source) at the Geoscience Center of the University Göttingen. Sample powders were hand-pressed in 3 mm drill holes in an acrylic sample holder. The analyzed area map was 1 mm^2 and the focus area was 20 μm. The results are presented as oxide wt% normalized to 100% (Table 2). Uncertainties range up to a few percent for some of the major elements, particularly Mg and Na and include the propagated uncertainty from calibration curves obtained from the μXRF measurement of 10 geostandards (AGV-2, Allende CV3, BCR-2, BHVO-2, BIR-1a, DTS-2b, GSP-2, SBC-1, STM-2, W-2A) that span a wide range of bulk elemental compositions and were run at the same measurement conditions as the CAI powders. Although some of the uncertainties are relatively large, the data quality is sufficient for investigating CAI pre-accretionary irradiation effects. The chemical composition of the forsterite-bearing CAI *Alvin* was analyzed before by Bullock et al. (2012) using EMPA spot analysis. Their reconstructed bulk composition of *Alvin* is in good agreement with the

TABLE 2. Chemical composition and grayscale values of the 17 analyzed Allende CV3 CAIs and the two test samples.

Sample	SiO_2	TiO_2	Al_2O_3	Fe_2O_3	MnO	MgO	CaO	Na_2O	K_2O	P_2O_5	Grayscale
Alvin	38.0 ± 2.9	1.10 ± 0.16	16.2 ± 2.6	0.9 ± 1.5	0.02 ± 0.03	24.7 ± 2.4	19.1 ± 0.9	0.03 ± 0.55	0.02 ± 0.29	0.02 ± 0.13	43.7
CGft-3	34.1 ± 2.9	0.40 ± 0.16	25.7 ± 2.8	8.4 ± 1.5	0.07 ± 0.03	14.9 ± 2.3	11.4 ± 0.7	4.79 ± 0.54	0.16 ± 0.28	0.00 ± 0.13	42.1
CGft-5	24.8 ± 3.0	1.64 ± 0.16	27.4 ± 2.8	0.7 ± 1.5	0.01 ± 0.03	8.8 ± 2.2	36.6 ± 1.3	0.00 ± 0.55	0.00 ± 0.29	0.09 ± 0.13	57.8
CGft-6	28.4 ± 3.0	2.25 ± 0.17	26.8 ± 2.8	0.2 ± 1.6	0.00 ± 0.03	10.0 ± 2.3	32.3 ± 1.2	0.00 ± 0.55	0.00 ± 0.29	0.04 ± 0.13	52.0
CGft-7	24.1 ± 3.0	0.79 ± 0.16	33.2 ± 3.0	1.6 ± 1.5	0.01 ± 0.03	8.1 ± 2.2	32.1 ± 1.1	0.05 ± 0.55	0.00 ± 0.29	0.06 ± 0.13	47.9
CGft-8	33.3 ± 2.9	0.72 ± 0.16	25.1 ± 2.8	7.5 ± 1.5	0.07 ± 0.03	11.4 ± 2.3	20.9 ± 0.9	1.04 ± 0.54	0.03 ± 0.29	0.05 ± 0.13	47.6
CGft-10	36.0 ± 2.9	1.84 ± 0.17	24.4 ± 2.7	0.6 ± 1.5	0.01 ± 0.03	10.1 ± 2.3	27.0 ± 1.0	0.00 ± 0.55	0.00 ± 0.29	0.04 ± 0.13	47.8
CGft-11	29.0 ± 3.0	1.66 ± 0.16	24.2 ± 2.7	0.1 ± 1.6	0.01 ± 0.03	12.4 ± 2.3	32.6 ± 1.2	0.00 ± 0.55	0.00 ± 0.29	0.07 ± 0.13	54.4
CGft-12	25.9 ± 3.0	1.58 ± 0.16	32.0 ± 3.0	1.2 ± 1.5	0.01 ± 0.03	5.0 ± 2.2	33.9 ± 1.2	0.28 ± 0.55	0.00 ± 0.29	0.06 ± 0.13	54.8
CGft-13	30.2 ± 2.9	1.49 ± 0.16	25.0 ± 2.8	0.4 ± 1.6	0.01 ± 0.03	9.6 ± 2.3	33.2 ± 1.2	0.00 ± 0.55	0.00 ± 0.29	0.07 ± 0.13	50.1
CGft-13Alt	30.1 ± 2.9	2.43 ± 0.17	24.3 ± 2.7	0.9 ± 1.5	0.01 ± 0.03	10.3 ± 2.3	31.9 ± 1.1	0.00 ± 0.55	0.00 ± 0.29	0.09 ± 0.13	49.3
FGft-12	37.0 ± 2.9	0.45 ± 0.16	26.0 ± 2.8	7.4 ± 1.5	0.06 ± 0.03	11.6 ± 2.3	10.7 ± 0.7	6.37 ± 0.55	0.36 ± 0.28	0.01 ± 0.13	36.7
FGft-13	32.3 ± 2.9	0.40 ± 0.16	27.2 ± 2.8	9.0 ± 1.5	0.11 ± 0.03	6.5 ± 2.2	20.1 ± 0.9	4.31 ± 0.53	0.12 ± 0.29	0.03 ± 0.13	49.7
FGft-17	35.2 ± 2.9	0.34 ± 0.16	23.8 ± 2.7	12.4 ± 1.6	0.11 ± 0.03	9.0 ± 2.2	12.4 ± 0.7	6.41 ± 0.55	0.36 ± 0.28	0.02 ± 0.13	43.8
FGft-19	36.1 ± 2.9	0.57 ± 0.16	26.5 ± 2.8	9.8 ± 1.5	0.08 ± 0.03	8.9 ± 2.2	11.9 ± 0.7	5.78 ± 0.55	0.35 ± 0.28	0.01 ± 0.13	47.3
FGft-23	37.4 ± 2.9	0.46 ± 0.16	23.1 ± 2.7	11.5 ± 1.5	0.10 ± 0.03	8.2 ± 2.2	12.8 ± 0.7	6.02 ± 0.55	0.35 ± 0.28	0.01 ± 0.13	46.4
FGft-25	34.1 ± 2.9	0.43 ± 0.16	26.1 ± 2.8	8.1 ± 1.5	0.06 ± 0.03	11.9 ± 2.3	15.9 ± 0.8	3.12 ± 0.53	0.26 ± 0.28	0.03 ± 0.13	46.0
FGft-27	32.7 ± 2.9	3.88 ± 0.20	26.3 ± 2.8	9.0 ± 1.5	0.05 ± 0.03	9.0 ± 2.2	13.3 ± 0.8	5.35 ± 0.54	0.45 ± 0.28	0.01 ± 0.13	46.8
Test1	35.4 ± 2.9	0.16 ± 0.16	2.8 ± 2.7	24.4 ± 2.0	0.12 ± 0.03	33.3 ± 2.6	2.6 ± 0.7	1.07 ± 0.54	0.07 ± 0.29	0.00 ± 0.13	47.4
Test2	27.3 ± 3.0	0.15 ± 0.16	3.4 ± 2.7	44.1 ± 3.0	0.34 ± 0.03	22.2 ± 2.4	1.6 ± 0.7	0.69 ± 0.54	0.04 ± 0.29	0.25 ± 0.12	82.3

results obtained here. Differences outside the given uncertainties exist for (ratio Bullock et al., 2012; this study) Al_2O_3 (1.25), MgO (1.17), and CaO (0.85). These differences are likely due to the limitation of obtaining the bulk composition from EMPA spot analysis. By integrating the individual spot data, it is usually assumed that 2-D surface data correspond to 3-D bulk data, which might not necessarily be true. In addition, slight sample heterogeneities might exist between the two *Alvin* subsamples investigated in the two studies.

The same aliquots were used for μXRF and noble gas studies. This raises the question of whether μXRF affects the noble gas budget of the samples. The dosage calculated via acceleration voltage and current of μXRF studies is similar to or lower than the dosage for μCT studies; for the latter, we already demonstrated that there is no effect on the noble gas budget (Parastoo et al. 2023), and hence, we infer that any such effect is also absent during μXRF.

μCT Measurements (grayscales)

All samples were analyzed using μCT, which is a three-dimensional rapid and nondestructive imaging method. In recent research, μCT has emerged as a powerful technique for studying extraterrestrial objects like meteorites, micrometeorites, interplanetary dust particles (IDPs), and material from sample return missions (e.g., Ebel & Rivers, 2007; Ebel et al., 2007; Friedrich et al., 2008; Hezel & Palme, 2010; Kadlag et al., 2023; Kuebler et al., 1999; Nettles & McSween Jr., 2006; Okazawa et al., 2002; Tsuchiyama, Nakamura, et al., 2002, Tsuchiyama, Shigeyoshi, et al., 2002). By using μCT techniques, it is possible to obtain valuable insights into the structure of meteorites, including details about their internal structure as well as their chemical composition. (e.g., Jäggi et al., 2023; Kadlag et al., 2023; Uesugi et al., 2010).

The 19 extracted and powdered samples (17 CAIs and two test samples) were irradiated using a SkyScan 1174 micro-CT system (Bruker microCT, Kontich, Belgium) at the Department of Space Science and Planetology at the University of Bern. The irradiation parameters of the system were optimized for accurate visualization without altering the internal structure of the CAIs. We used clear glass and plastic sample vials for irradiation. To prevent any movement of the sample vial during imaging, a small amount of plasticene clay was used to fix the sample vial onto the holder bearing. All samples were irradiated at a voltage of 50 kV with a current of 800 μA in 19 4 h shifts. For more information, see Table 3. The projected images on the scintillator were recorded by a 1.3 Mpixel CCD camera with a lens having a 1:6 zoom range. Since the samples are small, we used a reduced region of interest (ROI). For one single projection, we used an exposure time of 280 ms (at 50 kV).

TABLE 3. Acquisition parameters used for the μCT analyses of the CAI samples.

Source voltage (kV)	50	Angular step (°)	0.2
Source current (μA)	800	Frame averaging	2
Resolution (μm)	13.31	Sharpening (%)	40
Filter	No filter	Ring artifact correction (%)	4
Exposure time (ms)	280	Beam hardening correction (%)	20
Random movement	Off	Acquisition time (h)	4

We used the NRecon (Micro Photonics Inc.) and CTAn programs (Bruker®) for analyzing the CT images. Since we used an acceleration voltage of only 50 kV, there was significant X-ray absorption in the sample. Consequently, ring artifacts and beam hardening occurred. The latter happens when the X-ray beam passes through an object, causing low-energy photons to be more efficiently absorbed than high-energy photons. This effect is particularly prominent in objects with high density. Both effects, ring artifacts and beam hardening, were corrected using the software package CTAn.

The 3-D images obtained for each powdered CAI sample were reconstructed from stacked 2-D images. The latter are grayscale images in which the grayscale is a measure for the X-ray attenuation. Bright areas are areas of high attenuation, that is, heavier elements and/or higher density, and dark areas are regions of low attenuation. The grayscale values were calibrated to a value of 1 for air, that is, for the surrounding of the sample. Since all samples were analyzed in the same geometry, that is, same type of sample holder, same type of powder, and similar filling heights, the relative grayscale values are directly comparable. In such a set-up, the lower grayscale value for some samples relative to others cannot be due to density effects or different geometries but must be due to the chemical composition. Therefore, samples with a lower grayscale value are made of lighter elements than samples with a higher grayscale value. The grayscale values measured for the CAI powders vary between 37 and 58 (Table 2).

For the studied CAI samples, the grayscale depends essentially on the relative abundance of the light elements Mg, Al, and Si to the heavier elements Ca and Fe. Since the Al and Si concentrations in the CAI samples are relatively constant, the variation in the light elements is essential in Mg, which is a major target element for cosmogenic Ne production. It is obvious that the complex chemical composition of CAIs cannot be reduced to one single grayscale value (this was not the purpose of the μCT study). For measuring chemical

composition data, EDS and/or SEM analyses can obtain more information even on small samples. The basic idea behind the μCT study was to investigate whether there is a correlation between grayscale values and cosmogenic ^{21}Ne production rates. The grayscale values depend on the chemical composition of the samples in a similar way as the ^{21}Ne production rates and we will show below that there is indeed a reasonable correlation between the two. Note that this correlation is expected to only hold for similar samples. Different sample types having a completely different chemical composition might have a similar grayscale value but might have a completely different ^{21}Ne production rate. However, as long as similar sample types are studied, the correlation should hold.

For establishing the correlation, the ^{21}Ne production rates for the selected CAIs calculated using their individual chemical composition are compared to the grayscale values measured for each CAI (see below). For the current study, such a correlation is not necessary as the chemical composition for the individual CAIs is known, and therefore, individual production rates can be calculated. However, in future studies on smaller CAIs, the situation might be different and the noble gas data must be obtained on samples without chemical composition data. In such cases, the relationship between grayscale values and ^{21}Ne production rates is helpful as μCT images can be obtained nondestructively even from very small samples, and μCT irradiation has no measurable effect on the noble gas concentrations (Ghaznavi et al., 2023).

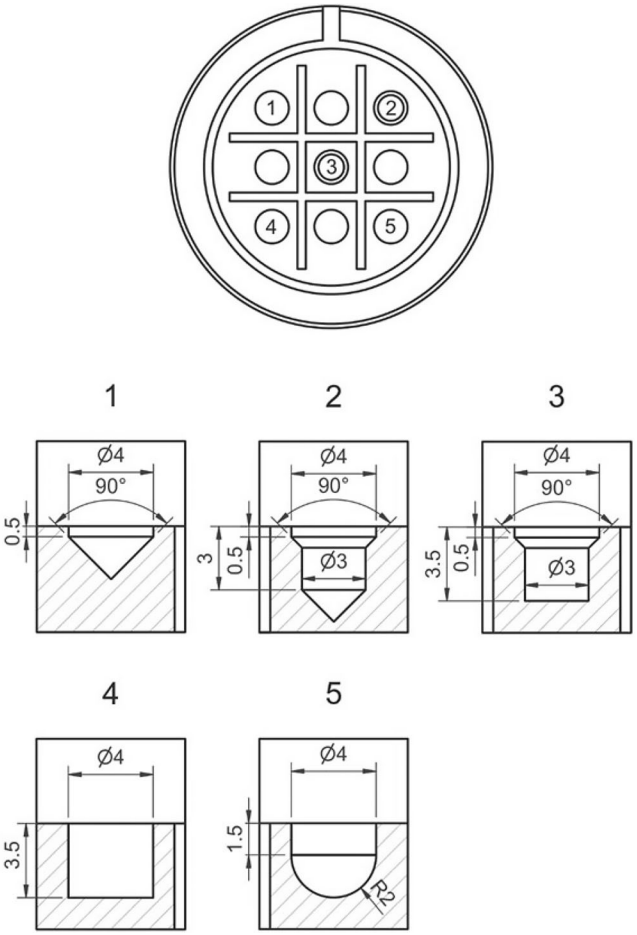

FIGURE 2. Different sample hole geometries tested for enhancing complete extraction of noble gases from small, highly refractory, powdered samples by laser melting.

Noble Gas Measurements

We measured the He, Ne, Ar, and Kr isotope concentrations in all CAIs and the two test samples. The powdered samples were gently pressed into the sample holes of an aluminum sample holder (one sample per hole) designed to minimize heating of neighbored samples during extraction, that is, choosing aluminum because of its relatively high thermal conductivity and designing a thick bottom plate to drain off most of the excess heat. To optimize the degassing of refractory samples, various sample hole geometries (various depths, flat, angle, or round bottom) were tested. An engineering drawing of the different setups is shown in Figure 2. Tests were performed using a powdered and homogenized bulk sample of Allende. Among all studied designs, number 2 was the most efficient for complete sample degassing and was therefore used in all further sample batches.

After loading, the samples were preheated at 80°C for about 20 h to release atmospheric surface contamination. One sample batch comprises five samples, blanks, and calibrations. Samples were degassed using an infrared diode laser having a continuous wavelength of 808 nm and a peak output power of 75 W (Type LM808, Dr. Mergenthaler, Germany). The laser head is connected to a two-color pyrometer. Since the laser spot is much smaller than the sample size, we systematically scanned over the sample to ensure complete degassing, and therefore, the extraction temperature and the extraction time were not the same for all samples. For a typical extraction, however, the temperature was about 2700°C for up to 15 min. For all samples, complete melting was observed (forming a melt droplet). In addition, we performed re-extractions at a slightly higher temperature and/or longer extraction time to ensure complete degassing.

The extracted noble gases were first cleaned using a water trap, which is an empty stainless steel U-tube cooled with liquid nitrogen (LN2). Even at the temperature of LN2, the tube is not trapping any noble gases but is efficiently trapping water. Next, the gas was further cleaned using SAES® getters working at a temperature of 280°C. Subsequently, the HeNe fraction was separated from the Ar/Kr/Xe fraction using a

charcoal held at the temperature of LN2. After the measurement of the HeNe fraction, the Ar/Kr/Xe fraction was released from the charcoal at 180°C and the Ar fraction was separated from the Kr/Xe fraction by freezing the latter into a charcoal held at a temperature of −125°C. After trapping Kr and Xe into the charcoal, the Ar fraction was trapped on a second charcoal trap held at a temperature of LN2. Parallel freezing at different temperatures makes the separation of Ar from Kr and Xe more efficient. Next, the Ar fraction was released from the charcoal at a temperature of 180°C and was measured after the HeNe fraction had been pumped out. Finally, the Kr/Xe fraction was released from the second charcoal at 180°C and was measured after the Ar fraction had been pumped out. Only the Kr in the Kr/Xe fraction was measured because the additional analysis of the Xe isotopes would have significantly increased the overall duration of the measurements, which in turn would have reduced the precision of the extrapolation of the Kr ion signals to the time of gas inlet. Measurements were done on an MAP 215-50 noble gas mass spectrometer, which is a single detector instrument with a channeltron working in counting mode and a Faraday Cup. The spectrometer has an improved detection system to increase the counting efficiency for heavy noble gases. The sensitivity of the MAP 215-50 is similar to the one of the noble gas mass spectrometer used by Vogel et al. (2003, 2004) but is significantly lower than the one of the mass spectrometer with a compressor source used by Kööp et al. (2018).

Each sample measurement was accompanied by at least one and up to six re-extractions, which were done by shooting the laser onto the sample with a slightly higher laser power and/or for a slightly longer time. The re-extractions contributed up to 25% to the total sample gas amounts (for ^{21}Ne) with the old sample holder geometry (design 4 in Figure 2) and they contributed on average ~1% (maximum 6%) to the total sample gas amounts using the improved design (design 2 in Figure 2).

In addition, we performed regular blank measurements by aiming the laser at an empty hole in the sample holder (therefore, only five out of a total of nine holes were used for samples, Figure 2). Finally, calibrations were performed regularly using calibration gas with atmospheric isotope composition for Ne, Ar, and Kr. The He calibration gas is enriched in ^{3}He relative to ^{4}He with respect to air. The results for He and Ne isotopes are summarized in Table 4; for Ar, the data are given in Table 5, and the results for Kr are given in Table 6.

MODEL CALCULATIONS OF COSMOGENIC PRODUCTION RATES

To identify any potential exposure signature, the CAIs might have acquired while free-floating in space after their formation, that is, before their accretion into the Allende parent body, it is imperative to first determine the ^{21}Ne production rates of the CAIs during their cosmic ray exposure in the Allende meteorite during its travel in space. Any indications for pre-accretionary exposure must be detected against this common base level. Using exposure models, these ^{21}Ne production rates can be calculated either based on the individual chemical composition and measured ^{22}Ne/^{21}Ne ratios or via the measured grayscale values and the measured ^{22}Ne/^{21}Ne ratios.

The basics of the model have already been described by Leya et al. (2021) and the model has already been used in the study by Tauseef et al. (2024). Briefly, the model is based on the particle spectra for primary and secondary particles and the cross sections for the relevant nuclear reactions. The new model version (U03) has some major improvements compared to earlier approaches (e.g., Leya & Masarik, 2009). First, the particle spectra are calculated using the Geant4 toolkit (e.g., Agostinelli et al., 2003). Second, the new model generation is the first to fully include primary and secondary galactic α-particles. *Third*, all relevant cross sections have been adjusted according to recent changes in AMS standards and/or half-lives, and *fourth*, the new model gives for the first time uncertainties. For more information, see Leya et al. (2021).

Using the new model, we calculated particle spectra for a carbonaceous chondrite with a radius of 65 cm (e.g., Nishiizumi et al., 1991) having the following chemical composition (wt%): H (<0.01%), C (0.29%), O (36.81%), Na (0.377%), Mg (15.05%), Al (1.76%), Si (16.02%), P (0.104%), S (2.02%), K (0.033%), Ca (1.88%), Ti (0.094%), Cr (0.33%), Mn (0.152%), Fe (23.59%), and Ni (1.43%) (e.g., Clarke et al., 1971; Fitzgerald, 1979; Jarosewich, 2006; McCarthy & Ahrens, 1972). This object is a good match for the carbonaceous chondrite Allende. Note that the choice of the chemical composition or the exact pre-atmospheric radius has only little influence on the calculated ^{21}Ne production rates. Since we are mostly interested in relative production rates, that is, production rates of one CAI relative to another CAI, the exact choice of the pre-atmospheric radius is not critical. The production rate differences among the studied CAIs would remain essentially unchanged for a slightly larger or a slightly smaller object. The absolute production rates, however, would change with radius.

Using the calculated particle spectra, the ^{21}Ne production rates and ^{22}Ne/^{21}Ne ratios were calculated for each CAI (and for the two test samples) using their individual chemical composition (Table 2). We have no information on the pre-atmospheric shielding depths of the studied CAIs because they are from different hand specimens. Since the ^{21}Ne production rate depends on

TABLE 4. Measured and cosmogenic He and Ne isotope concentrations in the FG- and CG-CAIs and two test samples.

		Concentrations in 10^{-8} $cm^3STP\,g^{-1}$						
Sample	Mass (mg)	^3He	^4He	^{20}Ne	$^{20}Ne/^{22}Ne$	$^{21}Ne/^{22}Ne$	$^{22}Ne/^{21}Ne_{cos}$	$^{21}Ne_{cos}$
Alvin	*14.56*	*7.78 ± 0.10*	*15,219 ± 124*	*2.460 ± 0.053*	*1.115 ± 0.035*	*0.865 ± 0.013*	*1.121 ± 0.020*	*1.906 ± 0.013*
CGft-3	[a]	—	—	—	—	—	—	—
CGft-5	[a]	—	—	—	—	—	—	—
CGft-6	11.74	[b]	17,981 ± 439	0.641 ± 0.444	0.410 ± 0.282	0.824 ± 0.028	1.214 ± 0.017	1.288 ± 0.028
CGft-7	14.79	7.37 ± 0.18	5102 ± 94	0.660 ± 0.167	0.450 ± 0.116	0.800 ± 0.020	1.250 ± 0.031	1.175 ± 0.016
CGft-8	*13.42*	*7.08 ± 0.16*	*5138 ± 95*	*1.855 ± 0.115*	*1.067 ± 0.074*	*0.793 ± 0.019*	*1.229 ± 0.029*	*1.377 ± 0.018*
CGft-10	14.36	5.82 ± 0.14	17,324 ± 299[c]	1.272 ± 0.302	0.853 ± 0.207	0.821 ± 0.017	1.215 ± 0.025	1.224 ± 0.014
CGft-11	15.92	5.34 ± 0.09	11,732 ± 149	1.020 ± 0.128	0.768 ± 0.100	0.840 ± 0.013	1.190 ± 0.018	1.116 ± 0.009
CGft-12	15.86	6.79 ± 0.07	12,153 ± 142	0.920 ± 0.047	0.711 ± 0.041	0.795 ± 0.022	1.258 ± 0.035	1.027 ± 0.022
CGft-13	15.37	8.38 ± 0.08	13,674 ± 147	1.318 ± 0.077	0.725 ± 0.047	0.843 ± 0.018	1.186 ± 0.025	1.533 ± 0.016
CG13ft-Alt	15.28	8.47 ± 0.18	14,057 ± 232	1.419 ± 0.050	0.758 ± 0.034	0.848 ± 0.024	1.179 ± 0.033	1.587 ± 0.029
FGft-12	10.47	5.80 ± 0.22	6995 ± 105	1.494 ± 0.042	0.698 ± 0.022	0.732 ± 0.014	1.366 ± 0.026	1.567 ± 0.015
FGft-13	10.03	6.27 ± 0.07	—[d]	1.100 ± 0.075	0.694 ± 0.048	0.732 ± 0.009	1.366 ± 0.017	1.160 ± 0.009
FGft-17	*9.49*	*4.32 ± 0.19*	*3750 ± 57*	*2.071 ± 0.304*	*1.210 ± 0.182*	*0.670 ± 0.022*	*1.432 ± 0.047*	*1.145 ± 0.011*
FGft-19	*13.08*	—[b]	*4164 ± 109*	*1.543 ± 0.310*	*0.967 ± 0.192*	*0.669 ± 0.012*	*1.473 ± 0.026*	*1.067 ± 0.012*
FGft-23	8.79	4.96 ± 0.09	3914 ± 63	1.822 ± 0.134	0.837 ± 0.066	0.692 ± 0.023	1.444 ± 0.048	1.506 ± 0.026
FGft-25	*8.66*	*5.87 ± 0.18*	*7074 ± 185*	*2.199 ± 0.115*	*1.109 ± 0.028*	*0.730 ± 0.010*	*1.329 ± 0.111*	*1.446 ± 0.011*
FGft-27	9.96	5.75 ± 0.07	26,444 ± 250	1.863 ± 0.790	0.796 ± 0.340	0.733 ± 0.029	1.364 ± 0.054	1.716 ± 0.035
Test1	8.06	6.83 ± 0.10	1165 ± 98	4.945 ± 0.291	1.973 ± 0.136	0.923 ± 0.014	0.949 ± 0.064	2.304 ± 0.011
Test2	11.64	7.39 ± 0.09	2563 ± 33	5.151 ± 0.183	2.176 ± 0.099	0.772 ± 0.013	1.107 ± 0.067	1.817 ± 0.016

Note: Values in italic indicate that the data might be affected by matrix contamination.
[a]Sample lost due to vacuum failure of the sample holder.
[b]^3He not measured due to technical problems.
[c]Second extraction not measured due to technical problems.
[d]^4He not measured due to technical problems.

shielding, we calculated average values. To be more specific, for calculating the particle spectra, we divided the 65 cm meteorite into 26 concentric shells, each with a thickness of 2.5 cm. The model therefore calculates 26 production rates, one for each shell, which are increasing from the surface (shell 1) toward the center (shell 26). The average production rate is then given by the average of the 26 individual values.

The calculated average production rates range from 0.235×10^{-8} $cm^3STP\,g^{-1}\,Myr^{-1}$ for *CGft-5* to 0.397×10^{-8} $cm^3STP\,g^{-1}Myr^{-1}$ for *Alvin*, that is, they vary by a factor of ~1.7. This large variation clearly demonstrates that using only one single production rate that has been calculated for an average chemical composition cannot be a reliable approach when searching for pre-irradiation effects. For the samples studied here, even assuming that all studied CAIs come from similar shielding conditions, we expect that the measured $^{21}Ne_{cos}$ concentrations among the studied CAIs vary by ~70%, simply due to variations in chemical composition (for the same irradiation time and the same irradiation geometry). For example, by ignoring this effect and simply using an average production rate, the (expected) higher $^{21}Ne_{cos}$ concentration for *Alvin* would be wrongly interpreted as a pre-irradiation effect because it would be ~70% higher than the (expected) $^{21}Ne_{cos}$ concentration for CAI *CGft-5*.

For the present study, we are in the comfortable situation that the chemical compositions of the studied CAIs are known, (Table 2) and therefore, individual production rates can be calculated (Table 7). In future studies, especially when studying smaller CAIs from other meteorite types, the chemical composition might not be known before the noble gas measurements. We therefore established a correlation between ^{21}Ne production rates and grayscale values for the studied CAIs (Figure 3, right panel). We expect this correlation to be applicable also to other CAIs from other carbonaceous chondrite types. Figure 3 depicts the calculated ^{21}Ne production rates as a function of grayscale values for the FG- (open symbols) and CG-CAIs (gray symbols). For each grayscale value, there is a range of ^{21}Ne production rates (shown by the array of symbols) that shows the range of data for the different depths in the meteorite. For example, the symbol at the lowest ^{21}Ne production rate (for a given grayscale value) corresponds to the pre-atmospheric surface of the meteorite and the symbols at the highest ^{21}Ne production

TABLE 5. Measured and cosmogenic Ar isotope concentrations in the FG- and CG-CAIs and two test samples.

	Concentrations in 10^{-8} $cm^3STP\ g^{-1}$				
Sample	^{38}Ar	$^{36}Ar/^{38}Ar$	^{40}Ar	$^{40}Ar/^{36}Ar$	$^{38}Ar_{cos}$
Alvin	*0.984 ± 0.024*	*1.22 ± 0.02*	*1428 ± 39*	*1111 ± 20*	*0.860 ± 0.046*
CGft-3[a]	—	—	—	—	—
CGft-5[a]	—	—	—	—	—
CGft-6	1.506 ± 0.089	1.47 ± 0.05	278 ± 17	134 ± 6	1.236 ± 0.127
CGft-7	1.996 ± 0.112	1.21 ± 0.02	1636 ± 94	720 ± 28	1.749 ± 0.148
CGft-8	*1.649 ± 0.106*	*2.41 ± 0.09*	*2389 ± 137*	*638 ± 1*	*1.023 ± 0.191*
CGft-10	1.498 ± 0.091	1.31 ± 0.05	671 ± 41	365 ± 1	1.281 ± 0.121
CGft-11	1.408 ± 0.071	1.16 ± 0.03	777 ± 72	88 ± 4	1.249 ± 0.095
CGft-12	1.708 ± 0.088	1.18 ± 0.03	1352 ± 91	563 ± 17	1.508 ± 0.118
CGft-13[b]	—	—	—	—	—
CG13ft-Alt	1.756 ± 0.091	1.17 ± 0.03	203 ± 14	76 ± 1	1.554 ± 0.121
FG-ft12	0.814 ± 0.016	5.81 ± 0.13	20,869 ± 400	4480 ± 100	[c]
FGft-13	1.243 ± 0.017	4.30 ± 0.07	7376 ± 129	1403 ± 30	0.270 ± 0.198
FGft-17	*0.812 ± 0.053*	*5.04 ± 0.35*	*11,063 ± 353*	*2745 ± 96*	*0.048 ± 0.156*
FGft-19	*0.752 ± 0.039*	*1.70 ± 0.31*	*20,795 ± 505*	*16,670 ± 2963*	*0.580 ± 0.064*
FGft-23	0.983 ± 0.019	9.85 ± 0.19	19,385 ± 189	2034 ± 27	[c]
FGft-25	*1.130 ± 0.024*	*5.32 ± 0.11*	*7898 ± 147*	*1344 ± 33*	*0.000 ± 0.226*
FGft-27	0.602 ± 0.031	1.72 ± 0.28	18,473 ± 608	16,629 ± 2608	0.462 ± 0.052
Test1	0.699 ± 0.017	5.34 ± 0.08	5437 ± 147	1356 ± 25	[c]
Test2	0.638 ± 0.014	4.33 ± 0.05	3630 ± 100	1224 ± 22	0.135 ± 0.104

Note: Values in italic indicate that the data might be affected by matrix contamination.
[a]Sample lost due to vacuum failure of the sample holder.
[b]Ar fraction lost due to technical problems.
[c]$^{38}Ar_{cos}$ cannot be determined due to excess ^{36}Ar caused by neutron capture.

TABLE 6. Measured Kr isotope data in FG- and CG-CAIs and two test samples.

	Concentration in 10^{-8} $cm^3STP\ g^{-1}$						
Sample	^{84}Kr	$^{78}Kr/^{84}Kr$[b]	$^{80}Kr/^{84}Kr$	$^{81}Kr/^{84}Kr$[b]	$^{82}Kr/^{84}Kr$	$^{83}Kr/^{84}Kr$	$^{86}Kr/^{84}Kr$
Air		*0.006087*	*0.03960*	—	*0.2022*	*0.2014*	*0.3052*
Alvin	*0.231 ± 0.024*	—	*0.080 ± 0.009*	*0.0008 ± 0.0017*	*0.220 ± 0.025*	*0.148 ± 0.019*	*0.285 ± 0.027*
CGft-3[a]	—	—	—	—	—	—	—
CGft-5[a]	—	—	—	—	—	—	—
CGft-6	0.501 ± 0.056	0.185 ± 0.037	0.050 ± 0.007	0.0073 ± 0.0022	0.199 ± 0.015	0.206 ± 0.016	0.283 ± 0.019
CGft-7	0.973 ± 0.124	0.023 ± 0.007	0.047 ± 0.006	0.0029 ± 0.0008	0.217 ± 0.029	0.215 ± 0.024	0.284 ± 0.035
CGft-8	*0.545 ± 0.057*	*0.192 ± 0.035*	*0.047 ± 0.006*	*0.0051 ± 0.0016*	*0.245 ± 0.017*	*0.225 ± 0.014*	*0.305 ± 0.026*
CGft-10	0.421 ± 0.046	0.075 ± 0.021	0.083 ± 0.009	0.0058 ± 0.0018	0.208 ± 0.017	0.188 ± 0.011	0.261 ± 0.028
CGft-11	1.028 ± 0.035	—	0.045 ± 0.002	0.0049 ± 0.0014	0.211 ± 0.009	0.205 ± 0.009	0.301 ± 0.011
CGft-12	0.829 ± 0.078	—	0.058 ± 0.007	0.0029 ± 0.0011	0.188 ± 0.019	0.211 ± 0.022	0.298 ± 0.037
CGft-13	0.573 ± 0.026	—	0.055 ± 0.004	0.0050 ± 0.0018	0.203 ± 0.013	0.203 ± 0.014	0.336 ± 0.041
CG13ft-Alt	0.374 ± 0.014	—	0.054 ± 0.003	0.0044 ± 0.0017	0.229 ± 0.012	0.235 ± 0.011	0.300 ± 0.017
FGft-12	0.474 ± 0.045	0.034 ± 0.030	0.345 ± 0.031	0.0092 ± 0.0030	0.300 ± 0.024	0.206 ± 0.015	0.301 ± 0.022
FGft-13	0.332 ± 0.066	0.018 ± 0.018	0.489 ± 0.047	0.0024 ± 0.0025	0.407 ± 0.041	0.218 ± 0.026	0.306 ± 0.029
FGft-17	*1.392 ± 0.091*	*0.009 ± 0.016*	*0.065 ± 0.009*	*0.0022 ± 0.0012*	*0.204 ± 0.023*	*0.195 ± 0.017*	*0.326 ± 0.029*
FGft-19	*1.088 ± 0.116*	—	*0.075 ± 0.008*	—	*0.219 ± 0.017*	*0.195 ± 0.017*	*0.291 ± 0.023*
FGft-23	0.645 ± 0.061	0.008 ± 0.004	0.818 ± 0.062	0.0013 ± 0.0009	0.523 ± 0.118	0.206 ± 0.012	0.329 ± 0.019
FGft-25	*0.608 ± 0.050*	—	*0.148 ± 0.020*	—	*0.241 ± 0.019*	*0.205 ± 0.013*	*0.307 ± 0.020*
FGft-27	0.259 ± 0.081	—	0.197 ± 0.047	0.0149 ± 0.0090	0.245 ± 0.064	0.211 ± 0.066	0.278 ± 0.072
Test1	0.259 ± 0.042	—	0.124 ± 0.024	0.0044 ± 0.0035	0.200 ± 0.043	0.184 ± 0.041	0.253 ± 0.054
Test1	0.311 ± 0.018	—	0.063 ± 0.008	0.0008 ± 0.0008	0.205 ± 0.020	0.229 ± 0.025	0.302 ± 0.024

Note: Values in italic indicate that the data might be affected by matrix contamination.
[a]Sample lost due to vacuum failure of the sample holder.
[b]^{78}Kr and ^{81}Kr are often below the detection limit, making the $^{78}Kr/^{84}Kr$ and $^{81}Kr/^{84}Kr$ ratios unreliable.

TABLE 7. $^{21}Ne_{cos}$ concentrations (10^{-8} $cm^3STP\,g^{-1}$), $^{21}Ne_{cos}$ production rates (10^{-18} $cm^3STP\,g^{-1}\,Myr^{-1}$), and modeled CRE ages (Myr) of FG- and CG-CAIs and two test samples.

		Grayscale		Direct	
Sample	$^{21}Ne_{cos}$	P(21,grayscale)	CRE age	P(21,direct)	CRE age
Alvin	*1.906 ± 0.013*	*0.330 ± 0.069*	*5.78 ± 1.12*	*0.397 ± 0.047*	*4.80 ± 0.57*
CGft-3[a]	—	0.344 ± 0.072	—	0.374 ± 0.041	—
CGft-5[a]	—	0.205 ± 0.043	—	0.235 ± 0.047	—
CGft-6	1.288 ± 0.028	0.256 ± 0.054	5.03 ± 1.07	0.249 ± 0.024	5.17 ± 0.51
CGft-7	1.173 ± 0.016	0.293 ± 0.061	4.00 ± 0.84	0.238 ± 0.021	4.93 ± 0.44
CGft-8	*1.377 ± 0.018*	*0.295 ± 0.062*	*4.67 ± 0.98*	*0.277 ± 0.028*	*4.97 ± 0.51*
CGft-10	1.224 ± 0.014	0.294 ± 0.062	4.16 ± 0.88	0.252 ± 0.024	4.86 ± 0.47
CGft-11	1.116 ± 0.009	0.235 ± 0.049	4.75 ± 0.99	0.271 ± 0.027	4.12 ± 0.41
CGft-12	1.027 ± 0.022	0.232 ± 0.049	4.43 ± 0.94	0.207 ± 0.016	4.96 ± 0.40
CGft-13	1.533 ± 0.016	0.273 ± 0.057	5.62 ± 1.17	0.243 ± 0.023	6.31 ± 0.60
CG13ft-Alt	1.587 ± 0.029	0.280 ± 0.059	5.67 ± 1.20	0.248 ± 0.024	6.40 ± 0.63
FGft-12	1.567 ± 0.015	0.392 ± 0.082	4.00 ± 0.84	0.366 ± 0.039	4.28 ± 0.46
FGft-13	1.160 ± 0.009	0.277 ± 0.058	4.19 ± 0.88	0.277 ± 0.027	4.19 ± 0.41
FGft-17	*1.145 ± 0.011*	*0.329 ± 0.070*	*3.48 ± 0.74*	*0.330 ± 0.035*	*3.47 ± 0.37*
FGft-19	*1.067 ± 0.012*	*0.298 ± 0.063*	*3.58 ± 0.76*	*0.327 ± 0.037*	*3.26 ± 0.37*
FGft-23	1.506 ± 0.026	0.306 ± 0.062	4.92 ± 1.00	0.316 ± 0.033	4.77 ± 0.50
FGft-25	*1.446 ± 0.011*	*0.309 ± 0.065*	*4.68 ± 0.99*	*0.317 ± 0.033*	*4.56 ± 0.48*
FGft-27	1.716 ± 0.035	0.302 ± 0.064	5.68 ± 1.21	0.317 ± 0.033	5.41 ± 0.57
Test1	2.304 ± 0.011	0.297 ± 0.064	7.76 ± 1.67	0.465 ± 0.061	4.95 ± 0.65
Test2	1.817 ± 0.016	—	—	0.321 ± 0.040	5.66 ± 0.71

Note: Values in italic indicate that the data might be affected by matrix contamination.
[a]Sample lost due to vacuum failure of the sample holder.

rates correspond to regions close to the pre-atmospheric center. The star shown for each sample is the average (see above). The ^{21}Ne production rates are in 10^{-8} $cm^3STP\,g^{-1}\,Myr^{-1}$. There is a reasonable linear correlation between ^{21}Ne production rates and the grayscale values, the best linear fit is:

$$P(^{21}Ne) = (7.17 \pm 0.77) \times 10^{-9} - (8.86 \pm 1.60) \times 10^{-11} \times \text{Grayscale}\left[\frac{10^{-8}\text{cm}^3\text{STP}}{\text{gMyr}}\right]$$

The deduced correlation holds for FG- and CG-CAIs as well as for CG-CAIs of type A and type B. Typical uncertainties for the ^{21}Ne production rates are ~20%. However, for this study, we are mostly interested in relative production rates, that is, the production rate of one CAI relative to another CAI. Considering only the uncertainties for the slope, the relative production rates have uncertainties in the range of ~18%. Assuming a CRE age for Allende of ~5 Myr (Scherer & Schultz, 2000), we would be able to detect an excess exposure of ~900 kyr (1σ relevance) or ~1.8 Myr (2σ relevance). This would be sufficient for finding pre-accretionary irradiation effects lasting ~1–2 Myr, which is just within the time span between CAI formation and chondrite parent body accretion (e.g., Piralla et al., 2023; Sugiura & Fujiya, 2014). With more data, that is, more CAIs with known chemical composition and measured grayscale values, the correlation could be improved, that is, could be made more precise, and consequently, the chances of detecting even shorter pre-irradiation effects could be improved. With the known chemical composition data, production rates can be calculated with an uncertainty of ~10%, which enable one to detect an excess exposure of ~500 kyr (1σ relevance) or ~1.0 Myr (2σ relevance). This clearly demonstrates how much such a study benefits from known measured chemical composition data.

Figure 3 (left panel) depicts the $(^{22}Ne/^{21}Ne)_{cos}$ ratios as a function of measured grayscale value. The question is, are the $(^{22}Ne/^{21}Ne)_{cos}$ ratios dominantly determined by the chemical composition of the studied CAIs or by shielding? For example, samples with higher than average Na concentrations would have—independent on shielding—high $(^{22}Ne/^{21}Ne)_{cos}$ ratios, because ^{22}Ne production from Na is very efficient. Indeed, because of their higher Na concentrations, FG-CAIs (open symbols) have on average higher $(^{22}Ne/^{21}Ne)_{cos}$ ratios than CG-CAIs (solid gray symbols). There is, however, no trend of $(^{22}Ne/^{21}Ne)_{cos}$ with grayscale. Instead, the large scatter of the data indicates that $(^{22}Ne/^{21}Ne)_{cos}$ is dominantly determined by the chemical composition, but not by the elements affecting the grayscale value. Therefore, differences in $(^{22}Ne/^{21}Ne)_{cos}$ among the different CAIs

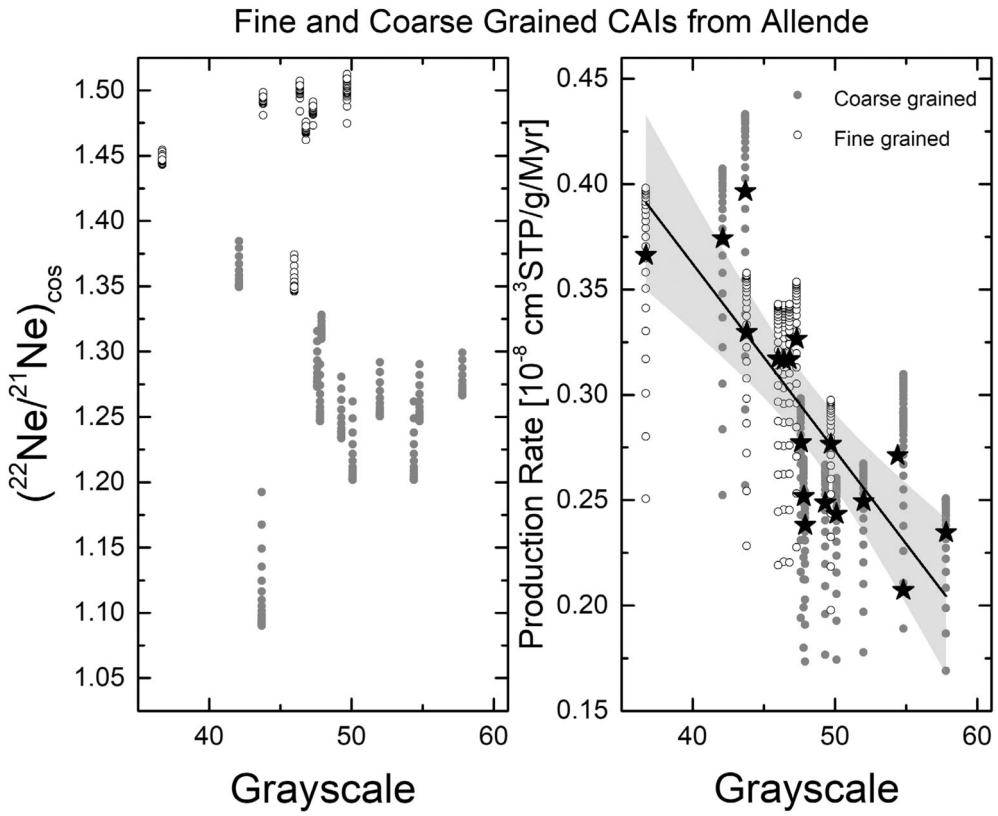

FIGURE 3. Modeled $(^{22}Ne/^{21}Ne)_{cos}$ as a function of grayscale values (left panel) and modeled $^{21}Ne_{cos}$ production rates as a function of grayscale values (right panel). For modeling the particle spectra, a CV carbonaceous chondrite with a pre-atmospheric radius of 65 cm is assumed. The production rates and production rate ratios are then calculated using the individual chemical composition of the CAIs.

cannot be interpreted with respect to shielding; a lower $(^{22}Ne/^{21}Ne)_{cos}$ ratio is no indication for higher shielding and therefore higher $^{21}Ne_{cos}$ production rates (as it is usually the case for meteorites of this size) but can simply be due to variations in chemical composition. Indeed, there is a slight trend of higher $(^{22}Ne/^{21}Ne)_{cos}$ ratios for samples with higher Na_2O concentrations.

RESULTS AND DISCUSSION OF THE NOBLE GAS DATA

This section summarizes the results for the He, Ne, Ar, and Kr isotope composition measured in the CAIs. Whenever possible, the results are compared to data from earlier work (e.g., Vogel et al., 2004).

Radiogenic ^4He and $^4He_{rad}$ Gas Retention

For calculating $^4He_{rad}$, we start with measured $^4He_{exp}$ and subtract cosmogenic $^4He_{cos}$. The latter has been calculated assuming all ^3He to be cosmogenic, which is reasonable considering that the measured Ne isotope ratios are all close to cosmogenic, and assuming $(^4He/^3He)_{cos} \sim 6$ (e.g., Alexeev, 1998; Leya & Masarik, 2009). In addition, we assume that trapped ^4He is zero, which is reasonable considering that CAIs were completely degassed during formation, and we also assume that there were no diffusive losses. The calculated $^4He_{rad}$ concentrations are summarized in Table 8. The radiogenic ^4He concentrations range from $(3884 \pm 63) \times 10^{-8}$ $cm^3STP\,g^{-1}$ for *FGft-23* to $(26{,}410 \pm 250) \times 10^{-8}$ $cm^3STP\,g^{-1}$ for *FGft-27*, that is, they vary by almost a factor ~7. Since $^4He_{rad}$ is from the radioactive decay of U and Th, the large variation in $^4He_{rad}$ indicates large variations in U and Th concentrations.

For calculating the expected total amount of $^4He_{rad}$, the U concentration, the Th/U ratio, and the CAI formation age must be known. For the latter, we use 4567 Myr. The percentage of retained $^4He_{rad}$ is then obtained by comparing the expected $^4He_{rad}$ concentrations to the measured $^4He_{rad}$ concentrations (Table 8). Doing so, the U concentrations were measured for all CAIs, but the Th concentrations were only measured for FG-CAIs (see Table 8). For the FG-CAIs, for which the calculations are straightforward, the data indicate complete or almost complete retention of $^4He_{rad}$. For the CG-CAIs, one must

TABLE 8. K, U, and Th concentrations, $^4He_{rad}$ and $^{40}Ar_{rad}$ concentrations, $^4He_{rad}$ retention rates, and K concentration calculated from $^{40}Ar_{rad}$.

Sample	^{4}He(rad) (10^{-8}cm^{3}STP g^{-1})	U-conc. (ppb)	Th-conc. (ppb)	^{4}He gas retention (%)[d]	^{40}Ar (rad) (10^{-8}cm^{3}STP g^{-1})	K-conc. from ^{40}Ar (rad) (ppm)[e]	K-concentration (ppm, measured)
Alvin	*15,172 ± 125*	*88.7*	*327**	*~98**	*1428 ± 39*	*170*	*200 ± 2900*
CGft-3[a]	—	—		—	—	—	1300 ± 2275
CGft-5[a]	—	106	392*	—	—	—	0 ± 2400
CGft-6	17,981 ± 439[b,c]	102	377*	~100*	278 ± 17	0	0 ± 2400
CGft-7	5058 ± 95	23.7	87.7*	~123*	1636 ± 94	205	0 ± 2400
CGft-8	*5095 ± 96*	*32*	*118**	*~100**	*2389 ± 137*	*300*	*200 ± 2400*
CGft-10	17,289 ± 300	98.7	365*	~100*	671 ± 41	85	0 ± 2400
CGft-11	11,700 ± 150	66.7	247*	~100*	777 ± 72	0	0 ± 2400
CGft-12	12,112 ± 142	69.7	258*	~100*	1352 ± 91	170	0 ± 2400
CGft-13	13,624 ± 147	76.2	382*	~103*	—	—	0 ± 2400
CG13ft-Alt	14,006 ± 233	—	—		203 ± 14	0	0 ± 2400
FGft12	6960 ± 106	10	226	>100	20,869 ± 400	2620	3000 ± 2300
FGft13	—	10	241	—	7376 ± 129	930	1000 ± 2400
FGft17	*3724 ± 58*	*3*	*415*	*58*	*11,063 ± 353*	*1390*	*3000 ± 2300*
FGft19	*4164 ± 109*[c]	*9*	*161*	*>100*	*20,795 ± 505*	*2610*	*2900 ± 2300*
FGft23	3884 ± 63	22	239	63	19,385 ± 189	2430	2900 ± 2300
FGft25	*7039 ± 186*	*8*	*343*	*>100*	*7898 ± 147*	*995*	*2200 ± 2300*
FGft27	26,410 ± 250	180	69	>100	18,473 ± 608	2320	3700 ± 2300
Test1	1124 ± 99	6.88 ± 0.60			5437 ± 147	685	600 ± 2400
Test2	2519 ± 34	15.4 ± 0.21			3630 ± 100	455	300 ± 2400

Note: Values in italics indicate that the data might be affected by matrix contamination.
[a]Sample lost due to vacuum failure of the sample holder.
[b]Second re-extraction is missing.
[c]No ^{3}He measurement, assuming all ^{4}He is radiogenic.
[d]Percentage of $^4He_{rad}$ retention calculated from U and Th concentrations and assuming a gas retention age of 4.567 Gyr.
[e]K concentrations calculated from $^{40}Ar_{rad}$ and assuming a gas retention age of 4.567 Gyr.
*Assuming Th/U ~ 3.7 for CG-CAIs.

make assumptions about the Th/U ratio. Brennecka et al. (2010, 2017) measured for five CG-CAIs from Allende Th/U ratios between 2.1 and 4.5. For two other CG-CAIs, however, the Th/U ratio was as high as 12.1. In an earlier study, Mason and Taylor (1982) determined Th/U ratios of 6.4 and 9.2 for two CG-CAIs. Excluding the two ratios >10 gives an average Th/U ratio for CG-CAIs of 4.5 ± 2.1. This ratio is essentially chondritic (Th/U ~ 3.7) and might be a good approximation for CAIs that have not suffered much U volatile losses. For calculating ^{4}He retention rates of the CG-CAIs, we assume Th/U ~ 3.7, consistent with most of the experimental data. Based on this Th/U ratio, the calculated $^4He_{rad}$ retention rates are between ~90% and ~ 120%, that is, essentially complete $^4He_{rad}$ retention for all studied CG-CAIs (Table 8). For *CG-ft-7*, the measured $^4He_{rad}$ concentration is higher than the calculated/expected concentration, giving a nominal retention rate of ~120%. For this CAI, assuming a Th/U ratio of ~6.5, that is, well within the range of measured ratios but consistent with a relatively low U concentration, brings measured and calculated $^4He_{rad}$ concentrations into agreement (with 100% retention). Our result for $^4He_{rad}$ is in line with Vogel et al. (2004), who also concluded that radiogenic ^{4}He has been retained in CV3 CAIs.

Cosmogenic Ne Isotopes—Excess ^{21}Ne in CAIs?

The results for Ne isotopes are summarized in Table 4 and the isotope ratios are shown in an Ne-three-isotope plot, that is, $^{20}Ne/^{22}Ne$ as a function of $^{21}Ne/^{22}Ne$, in Figure 4. Also shown are data for Allende CAIs from Vogel et al. (2004) (light gray diamonds) and data for matrix material, rim material, and dark inclusions from Allende (Vogel et al., 2003) (light gray squares). Most of the studied CAIs have $^{20}Ne/^{22}Ne$ and $^{21}Ne/^{22}Ne$ ratios in agreement with expected cosmogenic ratios. These CAIs also agree within the uncertainties with the earlier data on Allende CAIs from Vogel et al. (2004). Five samples, however, have $^{20}Ne/^{22}Ne$ ratios higher than the assumed cosmogenic endmember ($^{20}Ne/^{22}Ne$ in brackets); *Alvin* (1.115 ± 0.035), *CGft-8* (1.067 ± 0.074), *FGft-17* (1.210 ± 0.182), *FGft-19* (0.967

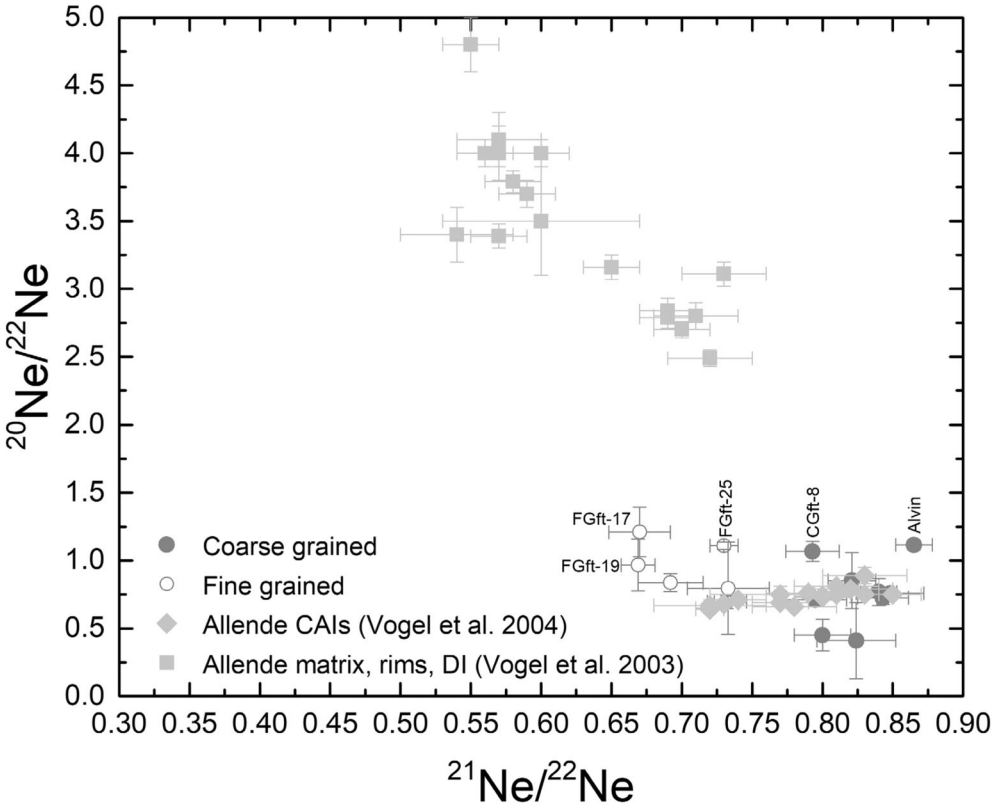

FIGURE 4. Ne-3-isotope plot showing the data for the coarse- and fine-grained CAIs. Also shown are the data for Allende CAIs from Vogel et al. (2004) and for Allende matrix, dark inclusions, and rim materials from Vogel et al. (2003).

± 0.192), and *FGft-25* (1.109 ± 0.028). The high $^{20}Ne/^{22}Ne$ ratios might indicate either remaining blank contributions (atmospheric Ne isotope composition) and/or matrix contamination, which would be a mixture of Ne-HL and Ne-Q (see Vogel et al., 2003 for data for Allende matrix material). Despite considering significant matrix contamination (more than 1%) unlikely (*Alvin* and *CGft-8* are very peculiar coarse-grained CAIs; *Alvin* is a forsterite-bearing CAI and *CGft-8* is a fluffy type A CAI with clear alteration features), contamination can nevertheless not completely be excluded. These five samples are therefore not discussed any further (also not for Ar and Kr). This leaves 11 of the 16 studied CAIs for further analysis. Note that *CGft-10* and *FGft-23* also have $^{20}Ne/^{22}Ne$ ratios slightly higher than the value of 0.83. However, considering that the cosmogenic $^{20}Ne/^{22}Ne$ endmember ratio is not that well constrained, we consider these samples still as reliable.

The cosmogenic $(^{22}Ne/^{21}Ne)_{cos}$ and $^{21}Ne_{cos}$ values are calculated using a two-component deconvolution assuming air ($^{20}Ne/^{22}Ne = 9.8$ and $^{21}Ne/^{22}Ne = 0.02878$) and cosmogenic ($^{20}Ne/^{22}Ne = 0.83$) as endmembers. For nine of the 16 CAI samples for which there are data, the measured $^{20}Ne/^{22}Ne$ ratios are lower than the assumed cosmogenic endmember of 0.83. For these samples, no corrections were applied. The uncertainties given for $^{21}Ne_{cos}$ and $(^{22}Ne/^{21}Ne)_{cos}$ are either the raw uncertainties from the noble gas measurements, including counting statistics, extrapolation of the signal back to the time of gas inlet, and corrections for blanks, interference, and fractionation, or half of the size of the correction applied for removing remaining air contamination, whatever is larger. The thus calculated uncertainties do not take into account systematic uncertainties and hence should not be used for inter-laboratory comparison of isotope ratios and gas concentrations. Typical systematic uncertainties are ~2% for isotope ratios and ~4% for gas concentrations. In this study, however, we are interested in differences in gas concentrations among samples measured with the same instrument, using the same calibration, and therefore, such systematic effects cancel out. For the following discussion, we also ignore the two test samples *Test1* and *Test2*.

The measured $^{21}Ne_{cos}$ concentrations range from $(1.027 \pm 0.022) \times 10^{-8}$ $cm^3STP\,g^{-1}$ for *CGft-12* to $(1.716 \pm 0.035) \times 10^{-8}$ $cm^3STP\,g^{-1}$ for *FGft-27*. There is no indication that $^{21}Ne_{cos}$ concentrations differ between CG- and FG-CAIs. The range measured here is in good

agreement with the range of ^{21}Ne concentrations (0.97×10^{-8} cm^{3}STP g^{-1}—1.72×10^{-8} cm^{3}STP g^{-1}) given by Vogel et al. (2004) for 19 CAIs from Allende. The $(^{22}Ne/^{21}Ne)_{cos}$ ratios vary between 1.179 ± 0.033 for *CGft-13-Alt* and 1.444 ± 0.048 for *FGft-23*. For $(^{22}Ne/^{21}Ne)_{cos}$ there is a trend of higher ratios for FG-CAIs than for CG-CAIs, which can be explained by the higher Na concentration of FG-CAIs (see Table 2 and discussion above). This is in agreement with the finding of Vogel et al. (2004) and indicates—but does not prove—that most of the cosmogenic Ne accumulated long after the secondary alteration event, that is, after the Allende meteoroid was released from its parent body.

Using Equation (1), we calculated ^{21}Ne production rates from measured grayscale values for the studied samples, P(21,grayscale). The results are given in Table 7. The production rates for the CAIs (10^{-8}cm^{3}STP g^{-1} Myr^{-1}) vary between 0.205 ± 0.043 and 0.392 ± 0.082, that is, the variation almost a factor of ~2. The large variation clearly demonstrates how important it is to correct for chemical composition when comparing gas concentrations of different CAIs (even from the same meteorite). We also calculated ^{21}Ne production rates directly by using the model calculations (see section Model Calculations of Cosmogenic Production Rates) and the individual chemical composition of the CAIs, P(21,direct) (see also Figure 3). The calculated production rates (in 10^{-8} cm^{3}STP g^{-1} Myr^{-1}) range from 0.235 to 0.366, that is, the variation is ~60% (Table 7). It is difficult to assign uncertainties to P(21,direct) because the modeled uncertainties for the different samples are highly correlated. The total uncertainty of the modeled ^{21}Ne production rates is expected to be in the range of 10%–15%. However, ratios of production rates, as used here, are more precise. In our case, however, the chemical compositions of the studied samples vary and thereby make uncertainty estimates even more challenging. Here, we assume a 5% uncertainty for P(21,direct). The maximum deviation between P(21,direct) and P(21, grayscale) is ~20% for *CGft-7*. Calculating the ratios between P(21,grayscale) and P(21,direct) for all CAIs and averaging the ratios gives a value of ~0.95, i.e., on average P(21,grayscale) is ~5% higher than P(21,direct). In this study, we are in the fortunate situation that we can calculate production rates directly for each CAI because we know their chemical composition. In future studies, however, when smaller CAIs from other meteorite types will be studied and no chemical composition data are available, the P(21,grayscale) values might provide a useful alternative.

Next, we divided the measured $^{21}Ne_{cos}$ concentrations by the ^{21}Ne production rates, thus calculating model CRE ages for each CAI. The ages are summarized in Table 7. Using P(21,grayscale), the ages range from 4.00 ± 0.84 Myr to 5.68 ± 1.21 Myr with no trend between FG- and CG-CAIs. For P(21,direct), the model ages range from 4.12 ± 0.41 Myr to 6.40 ± 0.63 Myr, again showing no trend with CAI type. The average deviation between ages calculated using P(21,grayscale) and P(21,direct) is ~5% (Table 7); the ages calculated via P(21,grayscale) are ~5% shorter than the ages calculated via P(21, direct). Note that the two samples, *CGft-13* and *CG13ft-Alt*, which are aliquots of the same CAI, yield identical CRE ages within uncertainties. This gives some confidence in the experimental data and in the data handling procedure.

Using the above data we, first, search for variations in CRE model ages among the studied CAIs, and, second, compare the CRE model ages to the known CRE age of the Allende meteorite. We start with a statistical interpretation of the individual CAI data. First, an outlier test was performed. Doing so, the first and third quartiles and the interquartile range iqr = 3rd quartile—1st quartile were calculated. From this, the upper and lower boundaries were calculated via upper = 3rd quartile + (1.5 × iqr) and lower = 1st quartile–(1.5 × iqr). All data above or below the upper and lower boundary, respectively, are considered outliers and merit further study. For the model ages calculated via P(21,grayscale), there are no outliers and the average model age is 4.77 ± 0.64 Myr. A similar result is obtained for the model ages calculated via P(21,direct); no outlier and an average CRE age of 5.04 ± 0.73 Myr. The averages are normal averages and the uncertainties are the 1σ standard deviations. To summarize, the outlier test indicates that the database is consistent and that there is no indication of excess $^{21}Ne_{cos}$ in any of the studied CAIs.

As a next step, we test whether the data are normally distributed, that is, whether they belong to one single distribution. If so, the data are consistent with the assumption that all studied CAIs experienced the same irradiation history, most likely within the Allende meteorite. The Shapiro–Wilk test for normal distributed data is applicable to sample sizes between 3 and ~ 50. Using the model ages calculated via P(21,grayscale), the Shapiro–Wilk test gives $W = 0.878$ and $p = 0.098$. For model ages calculated via P(21,direct) one obtains $W = 0.898$ and $p = 0.175$. Values of W close to 1 and $p > 0.05$ indicate that the data might be normally distributed. For example, a p-value of 0.805 indicates that the random sample, that is, the data, are with a probability of 80% from a normal distribution. Again, according to the test, there is no indication of excess $^{21}Ne_{cos}$ in any of the studied CAIs and the data therefore allow to calculate an average CRE age for the CAIs.

After having established that the data are normally distributed, we can calculate weighted averages and

compare the model CRE ages for the CAIs to the known CRE age for Allende. The weighted (using uncertainties as weights) average CRE model ages are 4.61 ± 0.29 Myr for ages calculated via P(21,grayscale) and 4.87 ± 0.19 Myr for ages calculated via P(21,direct), respectively. These ages are slightly shorter but still in agreement with the CRE age for Allende of 5.2 Myr given by Scherer and Schultz (2000).

Ne Data—Are There Any Indications for Ne-G?

In a recent study, Pravdivtseva et al. (2020) found indications for Ne-G in the fine-grained Allende CAI *Curious Marie*. The noble gas G component is thought to be material from the He burning shell of Red Giant AGB stars (e.g., Ott, 2014). Pure Ne-G can only be calculated from models of AGB stars, and the Ne isotope composition of presolar grains require mixing of Ne-G with other Ne from the star. The isotope ratios $^{20}Ne/^{22}Ne$ and $^{21}Ne/^{22}Ne$ in Ne-G are very low but are not well constrained. There are only upper limits available, but finite amounts of ^{20}Ne and ^{21}Ne are accompanying ^{22}Ne. Krypton from phase G shows large overabundances of isotopes made by the slow-neutron capture process. The G component of noble gases is carried by presolar grains of silicon carbide. It is usually accepted that CAIs formed close to the Sun in an environment too hot for presolar grains to survive. Pravdivtseva et al. (2020) presented strong evidence for an incorporated SiC grain in the *Curious Marie* CAI. In some of the temperature steps (1250–1300°C), there was a clear signal for Xe-G, hints of Kr-G, and a slight offset toward Ne-G. As already mentioned by Pravdivtseva et al. (2020), the Ne data alone provide only a weak argument because the $^{22}Ne/^{21}Ne$ ratios can also be explained as being a mixture of cosmogenic components produced from sodalite and melilite. Considering that *Curious Marie* is almost pure nepheline/sodalite (Pravdivtseva et al., 2020) due to the extensive alteration, high $^{22}Ne/^{21}Ne$ ratios are expected.

Figure 5a depicts a comparison of measured and modeled $(^{22}Ne/^{21}Ne)_{cos}$ ratios for the studied CG-CAIs. The modeled data are shown in a box plot, the stars show the minimum and maximum values, the box covers all data in-between the 25% and 75% quartiles, the small square shows the average of the data, and the horizontal line inside the box represents the median of the data. The gray bars shown for each CAI represent the experimental $(^{22}Ne/^{21}Ne)_{cos}$ ratios, showing the full 1σ standard deviation. Figure 5b depicts the data for FG-CAIs in the same type of diagram. All experimental $(^{22}Ne/^{21}Ne)_{cos}$ ratios (gray bars) agree with the model predictions or are lower than the model predictions (box plot). Therefore, all $(^{22}Ne/^{21}Ne)_{cos}$ ratios measured by us for the CAIs are fully consistent with cosmogenic production. In none of the studied CAIs are there any indications for excess ^{22}Ne due to incorporated SiC grains and therefore for the presence of Ne-G. Also Vogel et al. (2004) found no indications for trapped gases in their study of Allende CAIs. It is important to emphasize, however, that in the study by Pravdivtseva et al. (2020) the indication for an incorporated SiC grain in the *Curious Marie* CAI is based on the Xe isotope data; the Ne data alone are also not indicative for the existence of Ne-G and can fully be explained by cosmogenic Ne production from sodalite and melilite, as in our study and in the study by Vogel et al. (2004).

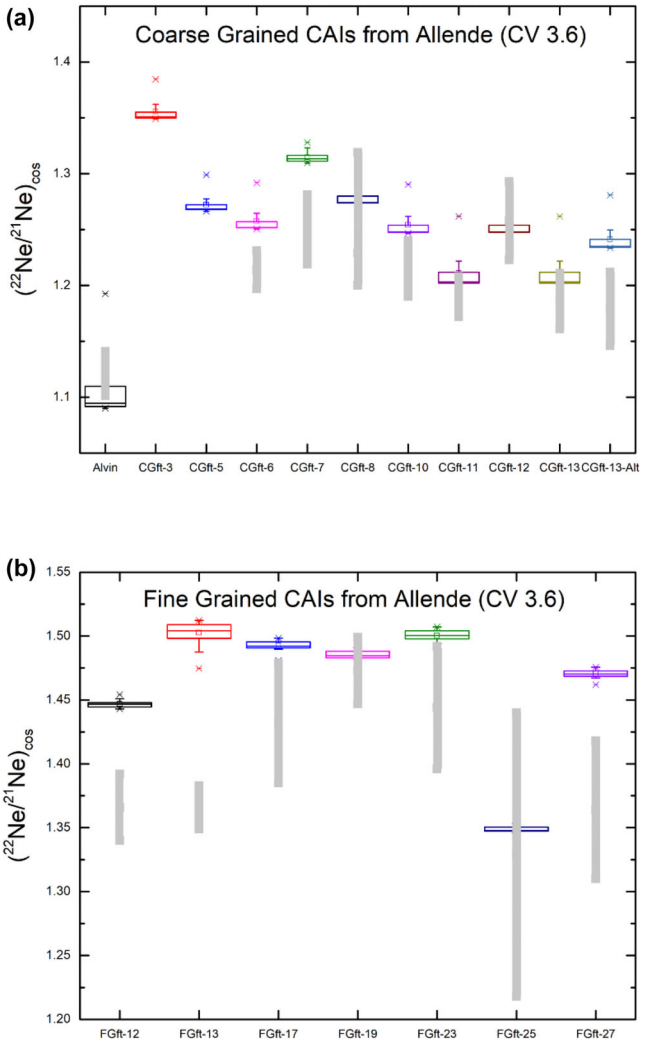

FIGURE 5. Comparison of measured and modeled $(^{22}Ne/^{21}Ne)_{cos}$ ratios for CG-CAIs (a) and FG-CAIs (b) CAIs from Allende. The modeled data are shown as a box plot, the stars show the minimum and maximum values, the box covers all data in-between the 25% and 75% quartiles, the small square shows the average of the data, and the horizontal line inside the box represents the median of the data. The gray bars shown for each CAI represent the experimental $(^{22}Ne/^{21}Ne)_{cos}$ ratios, showing the full 1σ standard deviation.

Cosmogenic and Radiogenic Ar Data

The Ar data are given in Table 5. The measured ^{38}Ar concentrations range from $(0.602 \pm 0.031) \times 10^{-8}$ $cm^3STP\ g^{-1}$ for *FGft-27* to $(1.996 \pm 0.112) \times 10^{-8}$ $cm^3STP\ g^{-1}$ for *CGft-7*, that is, the variation is more than a factor of 3. For most of the samples, measured $^{36}Ar/^{38}Ar$ ratios are below 5.32, indicating that there is cosmogenic Ar in the samples ($^{36}Ar/^{38}Ar_{cos} = 0.63$). For sample *FGft-25*, the $^{36}Ar/^{38}Ar$ ratio is within the uncertainties identical to trapped Ar, either planetary or (more likely) atmospheric contamination ($^{36}Ar/^{38}Ar_{tr} = 5.32$; e.g., Ott, 2014). Two samples, *FGft-12* and *FGft-23*, have $^{36}Ar/^{38}Ar$ ratios higher than the trapped endmember ($^{36}Ar/^{38}Ar = 5.81 \pm 0.13$ for *FGft-12* and 9.85 ± 0.19 for *FGft-23*) indicating excess ^{36}Ar.

Excess ^{36}Ar can be due to thermal neutron capture reactions on ^{35}Cl to produce ^{36}Cl, which then decays to ^{36}Ar. The target element Cl might be in the secondary mineral sodalite ($Na_8(Al_6Si_6O_{27})Cl_2$) or wadalite ($Ca_6(Al, Si,Mg)_7O_{16}C_{13}$), which might have been formed by aqueous alteration. If this is the case and the alteration involves Na-Cl-bearing fluids (e.g., Kimura & Ikeda, 1995; Tang et al., 2017), samples with excess ^{36}Ar should also be characterized by high Na abundances. Indeed, *FGft-12* and *FGft-23* both have relatively high Na concentrations (Table 2). In a broader sense, the Na concentration in FG-CAIs is on average higher than in CG-CAIs (Table 2), indicating a higher degree of alteration for the former than for the latter. In agreement with this, the $^{36}Ar/^{38}Ar$ ratios in FG-CAIs are on average higher than in CG-CAIs. To be more quantitative, the increase in Cl during alteration is expected to be accompanied by a decrease in Ca concentrations because melilite is replaced by sodalite and nepheline (e.g., Brearley & Jones, 1998). In this picture, samples with low Ca concentrations are more altered, have higher Cl concentrations, and therefore higher $^{36}Ar/^{38}Ar$ ratios. Figure 6a depicts the $^{36}Ar/^{38}Ar$ ratios as a function of CaO concentrations. There is indeed a trend of higher $^{36}Ar/^{38}Ar$ ratios for lower CaO concentrations, though there is significant scatter in the data. This scatter, however, is expected and can be explained by the fact that, for excess ^{36}Ar, not only high Cl concentrations but also high thermal neutron fluxes are necessary. The thermal neutron flux in a meteorite like Allende strongly depends on the shielding depth of the sample; it is highest close to the pre-atmospheric center and lowest close to the pre-atmospheric surface. Therefore, some samples might have a high Cl concentration (as shown by a high Na concentration) but might originate from lower shielding depths and are therefore not (or less) affected by thermal neutron capture effects. Consequently, it is well possible that at least some of the measured $^{36}Ar/^{38}Ar$ ratios are not affected by trapped Ar, but that the data can be explained by mixing the cosmogenic component with neutron capture produced Ar, which has $(^{36}Ar/^{38}Ar)_{nc} \sim 300$.

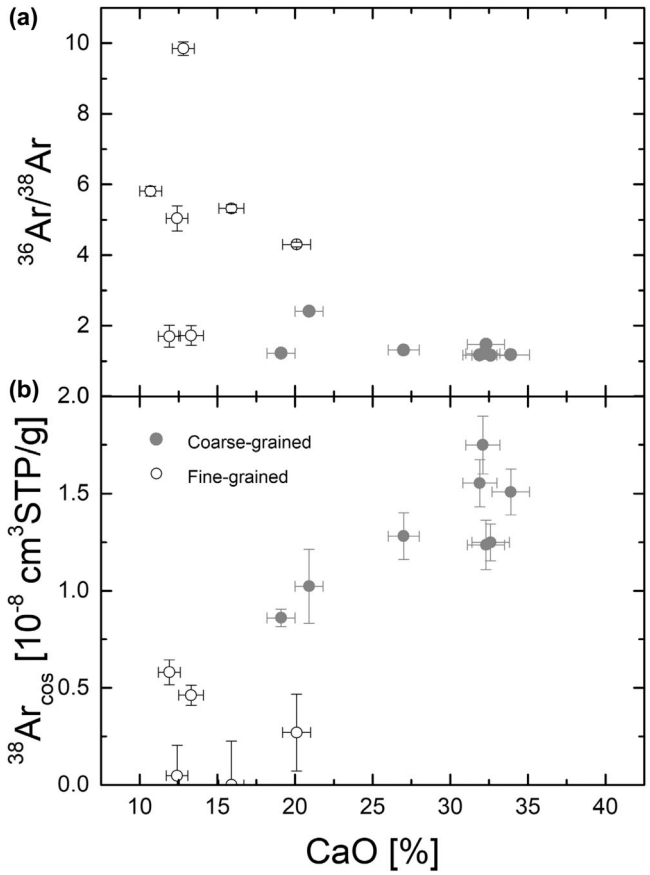

FIGURE 6. Measured $^{36}Ar/^{38}Ar$ ratios as a function of CaO concentration for coarse-grained CAIs (gray dots) and fine-grained CAIs (open circles) from the Allende meteorite (a). Cosmogenic ^{38}Ar concentrations as a function of CaO concentrations for the same samples.

Since cosmogenic ^{38}Ar is dominantly produced by spallation of Ca, the alteration event that increased Cl and reduced Ca would not only be detectable by higher $^{36}Ar/^{38}Ar$ ratios but also by lower $^{38}Ar_{cos}$ concentrations. Figure 6b depicts the $^{38}Ar_{cos}$ concentrations as a function of CaO concentrations. There is a clear trend that samples with higher $^{38}Ar_{cos}$ concentrations have higher CaO concentrations and vice versa. In summary, the data show a clear trend that FG-CAIs are more altered, have higher $^{36}Ar/^{38}Ar$ ratios, and lower $^{38}Ar_{cos}$ concentrations than the less altered CG-CAIs. Our data and the data interpretation agree with the study by Vogel et al. (2004).

The U-concentrations are supporting the discussion above. A high degree of aqueous metamorphism is often accompanied by loss of U, which becomes mobile when exposed to an oxidizing fluid (e.g., Langmuir, 1978; Tang

et al., 2017). On average, the U concentrations for the FG-CAIs are significantly lower than for the CG-CAIs (Table 8).

Cosmogenic ^{38}Ar concentrations show no correlation with $^{21}Ne_{cos}$, which is due to the significant dependence of $^{38}Ar_{cos}$ on the chemical composition. $^{38}Ar_{cos}$ varies with Ca concentration, that is, samples high in Ca have high $^{38}Ar_{cos}$ and samples low in Ca have low $^{38}Ar_{cos}$. The variation in $^{38}Ar_{cos}$ is more than a factor of 6 (only considering samples with no indications for matrix contamination, see above). In addition, also the $^{21}Ne_{cos}$ concentrations vary due to variable Mg, Al, and Si concentrations. However, the variation in $^{21}Ne_{cos}$ is only 50%, that is, much lower than the variation in $^{38}Ar_{cos}$. Consequently, since $^{38}Ar_{cos}$ strongly depends on the Ca concentration, but the model calculations for Ar isotopes from Ca are not well constrained, $^{38}Ar_{cos}$ is not useful for studying pre-irradiation effects in CAIs.

Assuming all ^{40}Ar to be radiogenic from ^{40}K decay and ^{40}Ar gas retention ages of 4.567 Gyr, we calculated the K concentrations needed to produce the measured $^{40}Ar_{rad}$ concentrations. For *CGft-6*, *CGft-11*, and *CGft-13-Alt*, the calculated K concentrations are zero because measured $^{40}Ar/^{36}Ar$ ratios are below 295, that is, below the ratio assumed for the trapped endmember. The highest $^{40}Ar_{rad}$ concentration is for *FGft-12*, which gives a K concentration of ~2620 ppm (Table 8). Note that the K concentrations might be slightly too large because some of the measured ^{40}Ar, which is assumed to be $^{40}Ar_{rad}$, might be ^{40}Ar from remaining terrestrial contamination. The calculated K concentrations agree with the chemically determined K concentrations (Table 2); though the latter have very high uncertainties, making this comparison less meaningful.

Like for $^{4}He_{rad}$, losses of $^{40}Ar_{rad}$ that occurred very early in solar system history, that is, within the first few kyr or Myr, would remain unnoticed. For example, complete loss of the small amount of $^{40}Ar_{rad}$ produced within the first 2 Myr would reduce the total $^{40}Ar_{rad}$ measured by us today only by ~0.1%, which would be undetectable considering the uncertainties involved in ^{40}Ar and K concentrations. Consequently, the finding of consistent $^{40}Ar_{rad}$ and K data is no proof of gas retention during early solar system alteration events.

Cosmogenic and Planetary Kr Data

The Kr isotopic data are compiled in Table 6 and are shown in Figures 7 and 8. Since some of the ^{78}Kr data are too high, likely due to unresolved hydrocarbon interferences, they are not discussed any further. The measured concentrations are low, being in the range of 10^{-11} cm^3STP for ^{84}Kr and 10^{-12} cm^3STP for ^{80}Kr, which explains the relatively large uncertainties. Figure 7

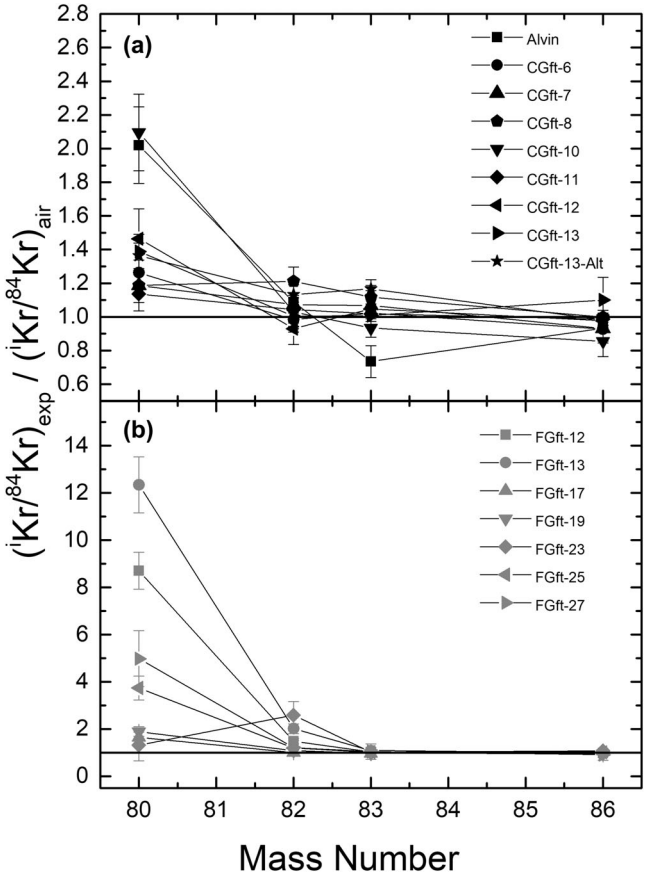

FIGURE 7. $Kr/^{84}Kr$ ($i = 80,82,83,86$) isotope ratios relative to atmospheric composition for coarse-grained (upper panel) and fine-grained (lower panel) CAIs from the CV 3.6 carbonaceous chondrite Allende.

depicts the Kr isotope ratios, normalized to ^{84}Kr, relative to terrestrial isotope ratios. In this plot, a value of 1 indicates that the measured ratio is identical to the terrestrial ratio, indicating that the measured ratio is indistinguishable from atmospheric contamination and/or blank. The results for the CG- and FG-CAIs are shown in a and b, respectively. For the CG-CAIs (panel a), all $^{80}Kr/^{84}Kr$ ratios deviate from terrestrial. For $^{82}Kr/^{84}Kr$, only sample *CGft-13-Alt* is slightly higher than terrestrial, though the differences disappear within the 2σ-uncertainties. For $^{83}Kr/^{84}Kr$, samples *CGft-10* and *CGft-13-Alt* deviate from terrestrial, but barely outside the 2σ uncertainties. The only significant deviation is for CAI *Alvin*, for which the $^{83}Kr/^{84}Kr$ ratio is lower than terrestrial by almost 3σ (Alvin is not discussed any further because of a likely matrix contamination, see above. As an alternative, Alvin could also contain some olivine). All studied CAIs have $^{86}Kr/^{84}Kr$ ratios in agreement with the terrestrial value.

For the FG-CAIs, all $^{80}Kr/^{84}Kr$ ratios are much larger than unity, indicating a clear ^{80}Kr excess. Most of

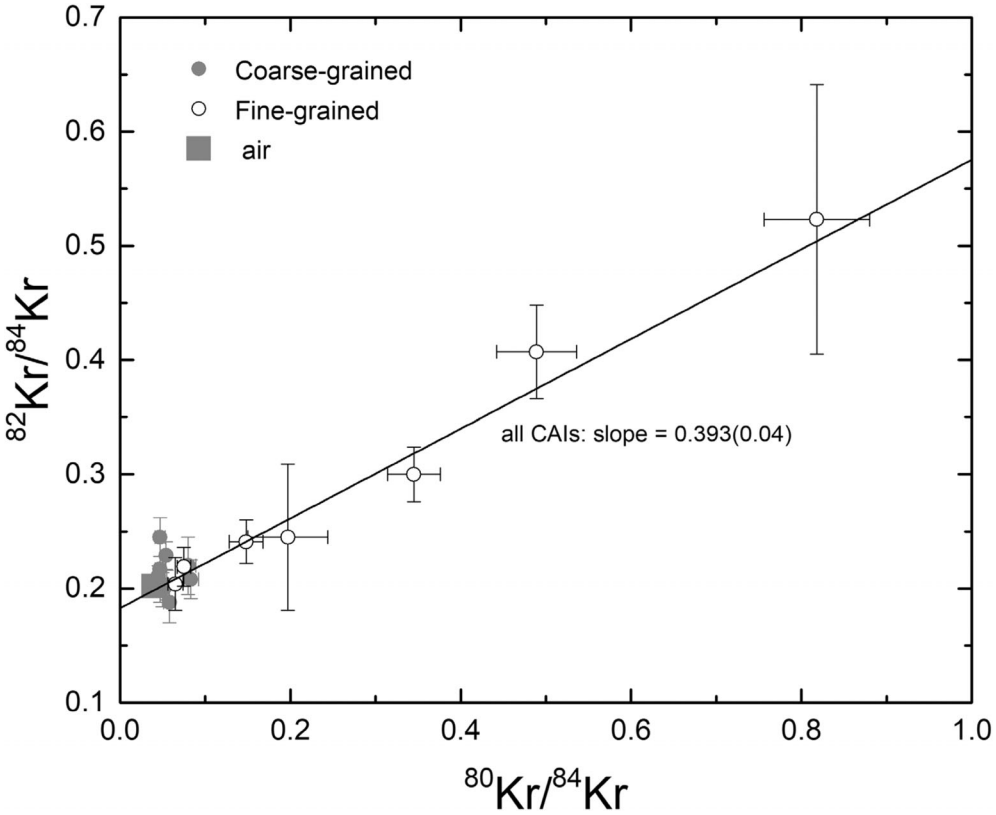

FIGURE 8. $^{82}Kr/^{84}Kr$ as a function of $^{80}Kr/^{84}Kr$ for fine- and coarse-grained CAIs from the CV 3.6 carbonaceous chondrite Allende. The linear correlation indicates ^{80}Kr and ^{82}Kr produced by neutron capture on Br.

the studied CAIs also show an excess in $^{82}Kr/^{84}Kr$, the only exceptions are *FGft-28* and *FGft-27*; however, the differences between measured and terrestrial ratios are just outside the 2σ uncertainties and are therefore considered as not relevant. For $^{83}Kr/^{84}Kr$ and $^{86}Kr/^{84}Kr$, all measured ratios agree within the uncertainties with their respective terrestrial ratios. In general, excesses in ^{80}Kr and ^{82}Kr are much larger for FG-CAIs than for CG-CAIs. For example, for the CG-CAIs, the highest $^{80}Kr/^{84}Kr$ ratio is ~2 times higher than terrestrial. In contrast, for FG-CAIs, the maximum $^{80}Kr/^{84}Kr$ ratio is more than 20 times higher than terrestrial.

To summarize, most of the Kr isotope ratios agree with the ratios for the terrestrial atmosphere, indicating that most of the Kr is (likely) atmospheric contamination and that there is no, or only very little cosmogenic Kr. Exceptions are the $^{80}Kr/^{84}Kr$ and $^{82}Kr/^{84}Kr$ ratios, which for all FG- and some of the CG-CAIs deviate from the terrestrial ratios. Figure 8 depicts measured $^{82}Kr/^{84}Kr$ as a function of $^{80}Kr/^{84}Kr$ for CG- and FG-CAIs. There is a clear linear trend between the ratios, indicating that both are affected by a similar or the same process, which is in this case neutron capture on Br. Thermal and epithermal neutron capture on ^{79}Br and ^{81}Br produces (after β-decay) ^{80}Kr and ^{82}Kr. Thermal neutron capture reactions are relatively common in carbonaceous chondrites, especially in carbonaceous chondrites of the size of Allende (pre-atmospheric radius ~ 65 cm, see also discussion of Ar isotopes). The slope of the correlation line is 0.393 ± 0.04, which is indistinguishable from the slopes of 0.3855 ± 0.0014 and 0.3837 ± 0.0017 given by Pravdivtseva et al. (2020) for the stepwise heating data of the Allende CAI *Curious Marie*.

None of the studied CAIs show any indications for ^{86}Kr excesses, which would be indicative for an *s*-process contribution as proposed by Pravdivtseva et al. (2020). However, as for the Ne isotopes (see above), small Kr-G contributions would remain undetectable in the one-temperature step approach. The finding that FG-CAIs have on average higher $^{80}Kr/^{84}Kr$ and $^{82}Kr/^{84}Kr$ ratios than CG-CAIs indicates that the former have on average higher Br concentrations than the latter. This is understandable, if Br is introduced into the CAIs by secondary alteration, and is in line with the discussion before for Na and Cl.

The main motivation for measuring Kr isotopes was to determine whether it is possible to also use the ^{81}Kr-Kr dating technique to search for pre-irradiation effects. The

advantage of this technique is that it largely corrects internally for shielding and its dependence on the chemical composition is only very minor. The idea is as follows. Starting with the equation from Leya et al. (2015), that is,

$$T = \frac{(0.43 \pm 0.02)}{\lambda_{81}} \times \left(\frac{^{83}\mathrm{Kr}}{^{81}\mathrm{Kr}}\right)_{\mathrm{cos}}$$

where λ_{81} is the ^{81}Kr decay constant (3.03 Myr^{-1}) (Baglin, 2008), the subscript "cos" denotes the cosmogenic component of the Kr isotopes, and the calculated CRE age T is expressed in Myr. The term $(^{83}\mathrm{Kr}/^{81}\mathrm{Kr})_{\mathrm{cos}}$ is the isotope ratio of cosmogenic ^{83}Kr to ^{81}Kr and the value (0.43 ± 0.02) is essentially the production rate ratio $\mathrm{P}(^{81}\mathrm{Kr})_{\mathrm{cos}}/\mathrm{P}(^{83}\mathrm{Kr})_{\mathrm{cos}}$, which is largely independent on shielding and chemical composition (Leya et al., 2015). However, for this technique to work, there must be clear cosmogenic signals for both ^{81}Kr and ^{83}Kr. Unfortunately, none of our samples show clear cosmogenic signals, neither for ^{81}Kr nor for ^{83}Kr, which is likely due to the small sample size. Consequently, for establishing the ^{81}Kr-Kr dating system to study pre-irradiation effects in CAIs, more material and/or a more sensitive mass spectrometer is needed. For an earlier approach, see also Vogel et al. (2009).

DISCUSSION

Depending on the hypothetical pre-accretionary irradiation scenario, different outcomes for a study like this could be predicted. First, pre-irradiation of CAIs before accretion into the chondrite parent bodies is not expected to be homogeneous for all CAIs. Instead, it is expected that some CAIs were irradiated for longer and/or more intensely than others before incorporation into the parent body. Consequently, some CAIs should have more $^{21}\mathrm{Ne}_{\mathrm{cos}}$ due to pre-compaction irradiation than others. One would therefore expect that all CAIs have a similar base level of $^{21}\mathrm{Ne}_{\mathrm{cos}}$ (if their different chemical compositions are considered) caused by their irradiation in the Allende meteoroid and that some (or all) CAIs have ^{21}Ne due to pre-accretion irradiation, but that such pre-irradiation signals are likely heterogeneous among the studied CAIs. One would not expect that all studied CAIs belong to a single normal distribution with no outliers. More intensely pre-irradiated CAIs would have more $^{21}\mathrm{Ne}_{\mathrm{cos}}$ and would therefore qualify as outliers. Second, if one imagines that the studied CAIs experienced very similar pre-accretion irradiation, that is, similar irradiation times at similar solar system locations, one would expect that the $^{21}\mathrm{Ne}_{\mathrm{cos}}$ concentrations in CAIs are relatively homogeneous but higher than the $^{21}\mathrm{Ne}_{\mathrm{cos}}$ concentration for the bulk meteorite (corrected for variations in chemical composition), that is, that the model CRE ages for the CAIs are higher than the model CRE age for the bulk meteorite.

We have shown that the cosmogenic Ne data are consistent with being from one single normal distribution without outliers. This finding enabled calculating weighted average model CRE ages of 4.61 ± 0.29 Myr (via P(21, gray)) and 4.87 ± 0.19 Myr (via P(21,direct)). The calculated model CRE ages for the studied CAIs agree with the accepted CRE age of Allende. Therefore, the data indicate that there was either no pre-irradiation or that there was a pre-irradiation, but that the entire pre-irradiation signal was lost during the early alteration event.

Despite the finding that the CRE ages are normally distributed, that there are no outliers, and that the model CRE ages for the CAIs agree with the CRE age for Allende, we nevertheless study whether CRE ages depend on the degree of alteration. The motivation for this is in the observation that there is significant scatter in the CRE ages. As can be seen in Table 7, the CRE ages range from 4.12 ± 0.41 Myr for *CGft-11* to 6.40 ± 0.63 Myr for *CGft-13-Alt*, that is, the variation is almost 60%. The question is as follows: Are the CRE ages longer for CAIs showing a lower degree of alteration than for CAIs showing a higher degree of alteration. If this is the case, longer CRE ages, that is, higher $^{21}\mathrm{Ne}_{\mathrm{cos}}$ concentrations, could indicate leftovers of a pre-accretionary irradiation signal that has not been (completely) erased by the early aqueous alteration event. If there is no such trend, then either there was no pre-irradiation or all of the pre-irradiation signatures were lost in all CAIs independent on their degree of aqueous alteration.

The following discussion is based on CRE ages calculated using P(21,direct). If some of the pre-irradiation effects would have been reduced (but not completely lost) by aqueous alteration, one would expect that CAIs that are more altered (high Na and low U concentrations) lost a larger part of pre-irradiation produced $^{21}\mathrm{Ne}_{\mathrm{cos}}$ than CAIs showing less effects for alteration (low Na and high U concentrations). We first assume that the Na_2O concentration is a measure for the degree of alteration because the target element Na is likely in the secondary mineral sodalite, that formed by aqueous alteration (e.g., Kimura & Ikeda, 1995; Tang et al., 2017). Figure 9a depicts the CRE ages as a function of measured Na_2O concentrations. There is no correlation between CRE ages and Na concentration, that is, with the degree of alteration. A similar test is possible by plotting the CRE ages as a function of U concentrations. A high degree of aqueous metamorphism is often accompanied by loss of U (e.g., Langmuir, 1978; Tang et al., 2017; see also above). Figure 9b depicts the

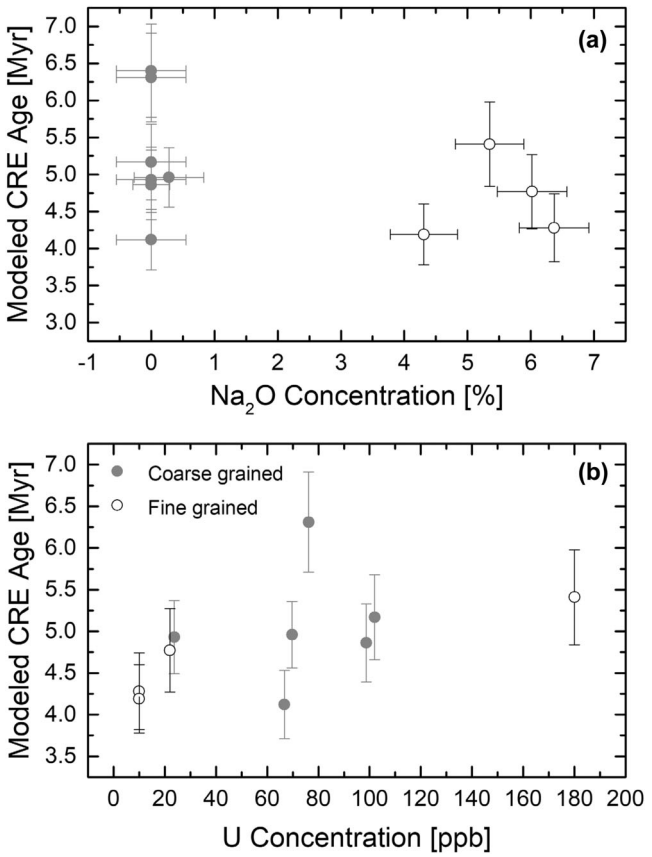

FIGURE 9. Modeled CRE ages for coarse- and fine-grained CAIs from the CV 3.6 carbonaceous chondrites Allende as a function of measured Na_2O concentrations (a) and U concentrations (b). Na_2O and U concentrations serve as a proxy for the degree of aqueous alteration. Not show are the data for *Alvin*, *CGft-8*, *FGft-17*, *FGft-19*, and *FGft-25*, which might be compromised by matrix contamination.

CRE ages as a function of U concentrations. Again, there is no trend between CRE ages and the degree of alteration.

While Figure 9 indicates that CRE ages show no trend with Na and U concentration and are therefore fully consistent with the hypothesis of either no pre-irradiation or complete loss of any pre-irradiation signal, a simple comparison of averages gives a slightly different picture. Calculating the weighted average CRE ages for FG- and CG-CAIs results in 4.56 ± 0.24 Myr and 5.04 ± 0.26 Myr, respectively, that is, the two ages agree within the 1σ standard deviation. The data, therefore, indicate that the more altered FG-CAIs have on average the same CRE age than the less altered CG-CAIs. Since most of our tests indicate that, first, the data measured for CAIs from Allende are normal distributed and show no clear trend with the degree of alteration and, second, the model CRE ages for the CAIs are similar to the CRE age for Allende, we conclude that either there was no pre-accretionary irradiation of the studied CAIs or that the signal caused by pre-accretionary irradiation, that is, excess $^{21}Ne_{cos}$, has been erased due to the early aqueous alteration event. However, taking alteration aside, we might speculate that our finding is at least not in favor of X-wind type models that launches CAIs on ballistic orbits above the disk (at least not for models that require repeated uplifts and/or that produce relatively long ballistic trajectories). Instead, the observations are consistent with the idea of CAI outward transport in an expanding disk (e.g., Yang & Ciesla, 2012).

CONCLUSIONS

This study searched for signatures caused by pre-accretionary irradiation in 17 CAIs from the CV 3.6 carbonaceous chondrite Allende. The results can be summarized as follows:

By combining physical model calculations for $^{21}Ne_{cos}$ production rates and $(^{22}Ne/^{21}Ne)_{cos}$ ratios in CAIs from Allende with measured He, Ne, Ar, and Kr isotope composition, the irradiation histories of the CAIs were studied. All CAIs show clear cosmogenic signals for He and Ne isotopes and most of the CAIs show cosmogenic signals for Ar isotopes. In addition, most samples show clear indications for $^{4}He_{rad}$ and some samples show indications for $^{40}Ar_{rad}$. For Kr isotopes, there are clear indications for ^{80}Kr and ^{82}Kr due to neutron capture on Br isotopes. All $(^{22}Ne/^{21}Ne)_{cos}$ ratios agree with the model predictions for the individual CAIs (fully considering their chemical composition), there is no indication for Ne-G, that is, for the existence of presolar SiC in any of the studied CAIs. However, indications for gases from SiC are difficult to detect if only Ne isotopes are considered and if gas extraction was in one temperature step.

The calculated CRE ages for the CAIs range between 4.12 ± 0.41 Myr and 6.40 ± 0.63 Myr (directly calculated production rates). Statistical tests indicate that the data are normally distributed with no outliers. The (weighted) average age is 4.87 ± 0.19 Myr. The data thus indicate that all CAIs share a common irradiation history, likely the irradiation in the Allende meteoroid. One could argue that CAIs *CGft-13* and *CGft13-Alt*, which are both part of the same CAI, have a longer CRE age than all the other studied CAIs and have also a longer CRE age than bulk Allende, which could indicate pre-accretionary exposure of this special CAI. However, all statistical tests indicate that CAI *CGft-13* is indistinguishable from the other CAIs.

There is no correlation between $^{21}Ne_{cos}$ concentrations and Na and/or U concentrations, the latter are indicators for the degree of aqueous alteration. The lack of correlation together with the finding of

normal distributed CRE ages that agree with the CRE age for Allende indicates that either none of the studied CAIs experienced pre-irradiation before parent body compaction and/or that any pre-irradiation effects would have been completely erased in the early solar system aqueous alteration event. The weighted average CRE age for the more altered FG-CAIs is slightly lower than the age calculated for less altered CG-CAIs. Since the difference is within the 1σ uncertainties and all other tests indicate no effect, we consider this slight difference as not significant.

Higher $^{36}Ar/^{38}Ar$, $^{22}Ne/^{21}Ne$, $^{80}Kr/^{84}Kr$, and $^{82}Kr/^{84}Kr$ ratios together with lower cosmogenic $^{38}Ar_{cos}$ and lower U concentrations in FG-CAIs compared to CG-CAIs are consistently explained by higher alteration of the former compared to the latter. In such alteration events, the target elements Na, Cl, and Br are added and Ca, which is a major target element for $^{38}Ar_{cos}$ production, is lost together with U.

Speculating that there was not a complete loss of pre-accretionary signatures due to the alteration event, the data indicate that there was no pre-accretionary irradiation of the studied CAIs. If true, the data contradict X-wind type scenarios (Figure 1a) because it is difficult to envision how to avoid GCR and/or SCR irradiation in such a ballistic event. In contrast, the data are supportive for scenarios considering CAI storage and transport in a turbulent disk with outward transport close to the midplane (Figure 1c), because in such a setup, CAIs are shielded from cosmic rays (Figure 1c). For scenarios assuming CAI storge in local high-density regions like spiral arms and/or gaps, the conclusion is not that clear (Figure 1b). Depending on the actual geometry, such regions might or might not be accessible to cosmic rays.

After having demonstrated that all the basics needed to search for pre-accretionary irradiation effects in CAIs are working reliably and that high quality data can be obtained, our future research focus in on the study of CAIs from less altered carbonaceous chondrites.

Acknowledgments—The CAIs studied in this work were generously provided by D. Ebel and S. Alpert at the American Museum of Natural History (all fine-grained CAIs + *CGft-3*), as well as Philipp Heck and James Holstein at the Robert A. Pritzker Center for Meteoritics and Polar Studies, Field Museum of Chicago (all remaining coarse-grained CAIs). We are grateful to Burkhard Schmidt (Georg-August-Universität Göttingen) for obtaining the μXRF data. This work was supported by the Swiss National Science Foundation (200020_196955, 200020_219357). FLHT is grateful for support from a Crosby Postdoctoral Fellowship (MIT) and a Packard Fellowship. We are grateful to A. Davis and an anonymous reviewer for careful and thorough reviews that helped improving the manuscript and to M.W. Caffee for editing.

Data Availability Statement—All relevant experimental data are given in the paper. The results of the model calculations and the microCT data can be found at the Harvard dataverse: https://doi.org/10.7910/DVN/FRGK4F.

Editorial Handling—Dr. Marc W. Caffee

REFERENCES

Agostinelli, S., Allison, J., Amako, K., Apostolakis, J., Araujo, H., Arce, P., Asai, M., et al. 2003. GEANT4—A Simulation Toolkit. *Nuclear Instruments and Methods in Physics Research A* 506: 250–313.

Alexeev, V. A. 1998. Parent Bodies of L and H Chondrites: Times of Catastrophic Events. *Meteoritics & Planetary Science* 33: 145–152.

Amelin, Y., Kaltenbach, A., Zsuyoshi, I., Stirling, C. H., Ireland, T. R., Petev, M., and Jacobsen, S. B. 2010. U-Pb Chronology of the Solar System's Oldest Solids with Variable $^{238}U/^{235}U$. *Earth and Planetary Science Letters* 300: 343–350.

Baglin, C. M. 2008. Nuclear Data Sheets for A = 81. *Nuclear Data Sheets* 109: 2257–2437.

Bollard, J., Connelly, J. N., Whitehouse, M. J., Pringle, E. A., Bonal, L., Jørgesen, J. K., Nordlund, A., Moynier, F., and Bizzarro, M. 2017. Early Formation of Planetary Building Blocks Inferred from Pb Isotopic Ages of Chondrules. *Science Advances* 6: e1700407.

Boss, A. P. 2008. Mixing in the Solar Nebula: Implications for Isotopic Heterogeneity and Large Scale Transport of Refractory Grains. *Earth and Planetary Science Letters* 268: 102–9.

Brearley, A. J., and Jones, R. H. 1998. Chondritic Meteorites. *Reviews in Mineralogy and Geochemistry* 36: 3-01 - 3-370.

Brennecka, G. A., Borg, L. E., Romaniello, S. J., Souders, A. K., Shollenberger, Q. R., Marks, N. E., and Wadhwa, M. 2017. A Renewed Search for Short-Lived 126Sn in the Early Solar System: Hybride Generation MC-ICPMS for High Sensitivity Te Isotope Analysis. *Geochimica et Cosmochimica Acta* 201: 331–344.

Brennecka, G. A., Weyer, S., Wadhwa, M., Janney, P. E., Zipfel, J., and Anbar, A. D. 2010. $^{238}U/^{235}U$ Variations in Meteorites: Extant ^{247}Cm and Implications for Pb-Pb Dating. *Science* 327: 449–451.

Bullock, E. S., MacPherson, G. J., Nagashima, K., Krot, A. N., Petaev, M. I., Jacobsen, S. B., and Ulyanov, A. A. 2012. Forsterite-Bearing Type B refractoryBre Inclusions from CV3 Chondrites: From Aggregates to Volatilized Melt Droplets. *Meteoritics & Planetary Science* 47: 2128–47.

Charlier, B. L. A., Tissot, F. L., Vollstaedt, H., Dauphas, N., Wilson, C. J. N., and Marquez, R. T. 2021. Survival of Presolar p-Nuclide Carriers in the Nebula Revealed by Step-Wise Leaching of Allende Refractory Inclusions. *Science Advances* 7.abf6222 https://doi.org/10.1126/sciadv.abf6222.

Ciesla, F. J. 2007a. Outward Transport of High-Temperature Materials around the Midplane of the Solar Nebula. *Science* 318: 613–15.

Ciesla, F. J. 2007b. Two-Dimensional Dynamics of CAIs in the Solar Nebula. In: *Workshop on Chronology of Meteorites*: 44-45.
Ciesla, F. J. 2010a. Residence Times of Particles in Diffusive Protoplanetary Disk Environments. I. Vertical Motions. *The Astrophysical Journal* 723: 514–529.
Ciesla, F. J. 2010b. The Distribution and Ages of Refractory Objects in the Solar Nebula. *Icarus* 208: 455–467.
Ciesla, F. J. 2011. Residence Times of Particles in Diffusive Protoplanetary Disk Environments. I. Radial Motions and Applications to Dust Annealing. *The Astrophysical Journal* 740: 9 (12 pp).
Ciesla, F. J., and Cuzzi, J. N. 2006. The Evolution of the Water Distribution in a Viscous Protoplanetary Disk. *Icarus* 181: 178–204.
Clarke, R. S., Jarosewich, E., Mason, B., Nelen, J., Gomez, M., and Hyde, J. R. 1971. The Allende, Mexico, Meteorite Shower. *Smithsonian Contributions to the Earth Sciences* 5: 1–53.
Cuzzi, J. N., Davis, S. S., and Dobrovolskis, A. R. 2003. Blowing in the Wind II. Creation and Redistribution of Refractory Inclusions in a Turbulent Protoplanetary Nebula. *Icarus* 166: 385–402.
Dauphas, N., and Schauble, E. A. 2016. Mass Fractionation Laws, Mass-Independent Effects, and Isotopic Anomalies. *Annual Review of Earth and Planetary Sciences* 44: 709–783.
Desch, S. J. 2007. Inti Did Not Form in an x-Wind (and neither Did Most CAIs) (Abstract) *Meteoritical & Planetary*. *Science* 42: 5073.
Desch, S. J., Dunlap, D. R., Dunham, E. T., Williams, C. D., and Mane, P. 2023. Statistical Chronometry of Meteorites. I. A Test of ^{26}Al Homogeneity and the Pb-Pb Age of the Solar system's $t = 0$. *Icarus* 402: 115607.
Ebel, D. S., Mey, J. L., and Rivers, M. L. 2007. Nondestructive Laser Confocal Scanning Microscopy and Synchrotron Microtomography of Single Stardust and Analog Tracks in Aerogel Keystones *38th Lunar and Planetary Science Conference*, LPI Contribution No. 1338.
Ebel, D. S., and Rivers, M. L. 2007. Meteorite 3-D Synchrotron Microtomography: Methods and Applications. *Meteoritics & Planetary Science* 42: 1627–46.
Fitzgerald, M. J. 1979. The Chemical Composition and Classification of the Karoonda Meteorite. *Meteoritics* 14: 109–115.
Friedrich, J. M., Wignarajah, D. P., Chaudhary, S., Rivers, M. L., Nehru, C. E., and Ebel, D. S. 2008. Three-Dimensional Petrography of Metal Phases in Equilibrated L Chondrites —Effects of Shock Loading and Dynamic Compaction. *Earth and Planetary Science Letters* 275: 172–180.
Fujiya, W., Sugiura, N., Hotta, H., Ichimura, K., and Sano, Y. 2012. Evidence for the Late Formation of Hydrous Asteroids from Young Meteoritic Carbonates. *Nature Communications* 3: 627. https://doi.org/10.1038/ncomms1635.
Fukuda, K., Tenner, T. J., Kimura, M., Tomioka, N., Siron, G., Ushikubo, T., Chaumard, N., Hertwig, A. T., and Kita, N. T. 2022. A Temporal Shift of Chondrule Generation from the Inner to Outer Solar System Inferred from Oxygen Isotopes and Al-Mg Chronology of Chondrules from Primitive CM and CO Chondrites. *Geochimica et Cosmochimica Acta* 322: 194–226.
Ghaznavi, P., Kadlag, Y., Haberthür, D., Hlushchuk, R., and Leya, I. 2023. Is μCT Irradiation Nondestructive? A Noble Gas Study on Matrix Samples from the CV3 Chondrite Allende. *Meteoritics & Planetary Science* 58: 897–900.
Grossman, L. 1972. Condensation in the Primitive Solar Nebula. *Geochimica et Cosmochimica Acta* 36: 597–619.
Grossman, L., Ebel, D. S., Simon, S. B., Davis, A. M., Richter, F. M., and Parsad, N. M. 2000. Major Element Chemical and Isotopic Composition of Refractory Inclusions in C3 Chondrites: The Separate Role of Condensation and Evaporation. *Geochimica et Cosmochima Acta* 64: 2879–94.
Grossman, L., Simon, S. B., Rai, V. K., Thiemens, M. H., Hutcheon, I. D., Williams, R. W., Galy, A., et al. 2008. Primordial Compositions of Refractory Inclusions. *Geochimica et Cosmochimica Acta* 72: 3001–21.
Haghighipour, N., and Boss, A. P. 2003a. On Pressure Gradients and Rapid Migration of Solids in a Non-uniform Solar Nebula. *The Astrophysical Journal* 583: 996–1003.
Haghighipour, N., and Boss, A. P. 2003b. On Gas-Drag Induced Rapid Migration of Solids in a Nonuniform Solar Nebula. *The Astrophysical Journal* 598: 1301–11.
Hezel, D. C., and Palme, H. 2010. The Chemical Relationship between Chondrules and Matrix and the Chondrule Matrix Complementarity. *Earth and Planetary Science Letters* 294: 85–93.
Hu, J. Y., Dauphas, N., Tissot, F. L. H., Yokochi, R., Ireland, T. J., Zhang, Z., Davis, A. M., et al. 2021. Heating Events in the Nascent Solar System Recorded by Rare Earth Isotopic Fractionation in Refractory Inclusions. *Science*. *Advances* 7: eabc2962.
Hutcheon, I. D., Marhas, K., Krot, A. N., Goswami, J. N., and Jones, R. H. 2009. ^{26}Al in Plagioclase-Rich Chondrules in Carbonaceous Chondrites: Evidence for an Extended Duration of Chondrule Formation. *Geochimica et Cosmochimica Acta* 73: 5080–99.
Itoh, S., Kojima, H., and Yurimoto, H. 2004. Petrography and Oxygen Isotopic Compositions in Refractory Inclusions from CO Chondrites. *Geochimica et Cosmochimica Acta* 68: 183–194.
Jäggi, N., Roth, A. S. G., Rüfenacht, M., Schönbächler, M., and Galli, A. 2023. Micro-XCT Chondrule Classification for Subsequent Isotope Analysis. *Meteoritics & Planetary Science* 58: 1039–55. https://doi.org/10.1111/maps.14026.
Jarosewich, E. 2006. Chemical Analysis of Meteorites and the Smithsonian Institution: An Update. *Meteoritics & Planetary Science* 41: 1381–82.
Kadlag, Y., Haberthür, D., Leya, I., Hlushchuk, R., and Mezger, K. 2023. Physical Properties and Average Atomic Numbers of Chondrules Using Computed Tomography. *Planetary and Space Science* 236: id. 105799.
Kimura, M., and Ikeda, Y. 1995. Anhydrous Alteration of Allende Chondrules in the Solar Nebula II: Alkali-Ca Exchange Reactions and Formations of Nepheline, Sodalite and ca-Rich Phases in Chondrules. *Antarctic Meteorite Research* 8: 123–138.
Kööp, L., Heck, P. R., Busemann, H., Davis, A. M., Greer, J., Maden, C., Meier, M. M. M., and Wieler, R. 2018. High Early Solar Activity Inferred from Helium and Neon Excesses in the Oldest Meteorite Inclusions. *Nature Astronomy* 2: 709–713.
Krot, A. N., Amelin, Y., Bland, P., Ciesla, F. J., Connelly, J., Davis, A. M., Huss, G. R., et al. 2009. Origin and

Chronology of Chondritic Components: A Review. *Geochimica et Cosmochimica Acta* 73: 4963–97.

Krot, A. N., Nagashima, K., Lyons, J. R., Lee, J. E., and Bizzarro, M. 2020. Oxygen Isotopic Heterogeneity in the Early Solar System Inherited from the Protosolar Molecular Cloud. *Science*. *Advances* 6: eaay2724.

Kuebler, K. E., McSween, H. Y., Carlson, W. D., and Hirsch, D. 1999. Sizes and Masses of Chondrules and Metal-Troilite Grains in Ordinary Chondrites: Possible Implications for Nebular Sorting. *Icarus* 141: 96–106.

Langmuir, D. 1978. Uranium Solution-Mineral Equilibria at Low Temperatures with Applications to Sedimentary Ore Deposits. *Geochimica et Cosmochimica Acta* 42: 547–569.

Larson, K. K., Trinquier, A., Paton, C., Schiller, M., Wielandt, D., Ivanova, M. A., Connelly, J. N., Nordlund, A., Krot, A. N., and Bizzarro, A. 2011. Evidence for Magnesium Isotope Heterogeneity in the Solar Protoplanetary Disk. *The Astrophysical Journal Letters* 735: L37 (7 pp).

Leya, I., Dalcher, N., Vogel, N., Wieler, R., Caffee, M. W., Welten, K. C., and Nishiizumi, K. 2015. Calibration of Cosmogenic Noble Gas Production Rates Based on ^{36}Cl-^{36}Ar Ages. Part 2. The ^{81}Kr-Kr Dating Technique. *Meteoritics & Planetary Science* 50: 1863–79.

Leya, I., Hirtz, J., and David, J.-C. 2021. Galactic Cosmic Rays, Cosmic-Ray Variations, and Cosmogenic Nuclides in Meteorites. *The Astrophysical Journal* 910: 136 (17 pp).

Leya, I., and Masarik, J. 2009. Cosmogenic Nuclides in Stony Meteorites Revisited. *Meteoritics & Planetary Science* 44: 1061–86.

Ma, C., Beckett, J. R., Tissot, F. L. H., and Rossmann, G. R. 2022. New Minerals in Type A Inclusions from Allende and Clues to Processes in the Early Solar System: Paqueite, $CA_3TiSi_2(Al,Ti,Si)_3O_{14}$, and Burnettite, $CaVAlSiO_6$. *Meteoritics & Planetary Science* 57: 1300–1324.

MacPherson, G. J., Bullock, E. S., Tenner, T. J., Nakashima, D., Kita, N. T., Ivanova, M. A., Krot, A. N., Petaev, M. I., and Jacobsen, S. B. 2017. High Precision Al-Mg Systematics of Forsterite-Bearing Type B CAIs from CV2 Chondrites. *Geochimica et Cosmochimica Acta* 201: 65–82.

MacPherson, G. J., Kita, N. T., Ushikubo, T., Bullocl, E. S., and Davis, A. M. 2012. Well-Resolved Variations in the Formation Ages for Ca-Al-Rich Inclusions in the Early Solar System. *Earth and Planetary Science Letters* 331: 43–54.

Mason, R., and Taylor, S. R. 1982. Inclusions in the Allende Meteorite. *Smithsonian Contributions to the Earth Sciences* 25: 30.

McCarthy, T. S., and Ahrens, L. H. 1972. Chemical Sub-Groups amongst HL Chondrites. *Earth and Planetary Science Letters* 14: 97–102.

McKeegan, K. D., Aléon, J., Bradley, J., Brownlee, D., Busemann, H., Butterworth, A., Chaussidon, M., et al. 2006. Isotopic Compositions of Cometary Matter Returned by Stardust. *Science* 314: 1724–28.

Nettles, J. W., and McSween, H. Y., Jr. 2006. A Comparison of Metal-Troilite Grain Size Distributions for Type 3 and Type 4 Ordinary Chondrites Using X-Ray CT Data. *37*th *Lunar and Planetary Science Conference*, abstract# 1996.

Nishiizumi, K., Arnold, J. R., Fink, D., Klein, J., and Middleton, R. 1991. ^{41}Ca Production Profile in the Allende Meteorite. Abstracts for the 54th Annual Meeting of the Meteoritical Society, LPI Contribution 766.

Okazawa, T., Tsuchiyama, A., Yano, H., Noguchi, T., Osawa, T., Nakano, T., and Uesugi, K. 2002. Measurement of Densities of Antarctic Micrometeorites Using X-Ray Microtomography. *Antarctic Meteorites NIPR* 11-13: 137–39.

Ott, U. 2014. Planetary and Pre-Solar Noble Gases in Meteorites. *Chemie der Erde* 74: 519–544.

Pape, J., Mezger, K., Bouvier, A.-S., and Baumgartner, L. P. 2019. Time and Duration of Chondrule Formation: Constraints from ^{26}Al-^{26}Mg Ages of Individual Chondrules. *Geochimica et Cosmochimica Acta* 244: 416–436.

Piralla, M., Villeneuve, J., Schnuriger, N., Bekaert, D. V., and Marrocchi, Y. 2023. A Unified Chronology of Dust Formation in the Early Solar System. *Icarus* 394: id. 115427.

Pravdivtseva, O., Tissot, F. L. H., Dauphas, N., and Amari, S. 2020. Evidence of Presolar SiC in the Allende Curious Marie Calcium-Aluminum-Rich Inclusions. *Nature Astronomy* 4: 617–624.

Richter, F. M., Davis, A. M., Ebel, D. S., and Hashimoto, A. 2002. Elemental and Isotopic Fractionation of Type B Calcium-, Aluminum-Rich Inclusions: Experiment, Theoretical Considerations, and Constraints on their Thermal Evolution. *Geochimica et Cosmochimica Acta* 66: 521–540.

Richter, F. M., Mendybaev, R. A., and Davis, A. M. 2006. Conditions in the Protoplanetary Disk as Seen by the Type B CAIs. *Meteoritics & Planetary Science* 41: 83–93.

Scherer, P., and Schultz, L. 2000. Noble Gas Record, Collisional History, and Pairing of CV, CO, CK, and Other Carbonaceous Chondrites. *Meteoritics & Planetary Science Letters* 35: 145–153.

Shu, F. H., Shang, H., and Lee, T. 1996. Towards an Astrophysical Theory of Chondrites. *Science* 271: 1545–52.

Siron, G., Fukuda, K., Kimura, M., and Kita, N. T. 2021. New Constraints from ^{26}Al-^{26}Mg Chronology of Anorthite Bearing Chondrules in Unequilibrated Ordinary Chondrites. *Geochimica et Cosmochimica Acta* 293: 103–126.

Sugiura, N., and Fujiya, W. 2014. Correlated Accretion Ages and ε^{54}Cr of Meteorite Parent Bodies and the Evolution of the Solar Nebula. *Meteoritics & Planetary Science* 49: 772–787.

Tang, H., Liu, M.-C., McKeegan, K. D., Tissot, F. L. H., and Dauphas, N. 2017. In Situ Isotopic Studies of the U-Depleted Allende CAI Curious Marie: Pre-Accretion Alteration and the co-Existence of ^{26}Al and ^{36}Cl in the Early Solar Nebula. *Geochimica et Cosmochimica Acta* 207: 1–18.

Tauseef, M., Leya, I., Gattacceca, J., Hofmann, B., Szidat, S., Braucher, R., and ASTER Team. 2024. ^{14}C and ^{14}C-^{10}Be Terrestrial Age Dating System for Meteorites – New Data for Four Recently Fallen Meteorites. *Meteoritics & Planetary Science* 59: 1219–35.

Tsuchiyama, A., Nakamura, T., Nakano, T., and Nakamura, N. 2002. Three-Dimensional Description of the Kobe Meteorite by Micro X-Ray CT Method: Possibility of Three-Dimensional Curation of Meteorite Samples. *Geochemical Journal* 36: 369–390.

Tsuchiyama, A., Shigeyoshi, R., Nakano, T., Uesugi, K., and Shirono, S. 2002. Three-Dimensional Shapes and Internal Structures of Chondrules from the Allende Meteorite by X-Ray CT: High-Speed Rotation. *Antarctic Meteorites NIPR* 11-13: 168–170.

Uesugi, M., Uesugi, K., and Oka, M. 2010. Non-destructive Observation of Meteorite Chips Using Quantitative Analysis of Optimized X-Ray Micro-Computed Tomography. *Earth and Planetary Science Letters* 299: 359–367.

Vogel, N., Baur, H., Bischoff, A., Leya, I., Roszjar, J., and Wieler, R. 2009. ^{81}Kr-Kr Dating to Detect Pre-Irradiation Effects in CAIs: Feasibility and First Results. 72nd Annual Meteoritical Society Meeting, #5320.

Vogel, N., Baur, H., Bischoff, A., Leya, I., and Wieler, R. 2004. Noble Gas Studies in CAIs from CV3 Chondrites: No Evidence for Primordial Noble Gases. *Meteoritics & Planetary Science* 39: 767–778.

Vogel, N., Wieler, R., Bischoff, A., and Baur, H. 2003. Microdistribution of Primordial Ne and Ar in Fine-Grained-Rims, Matrices, and Dark Inclusions of Unequilibrated Chondrites – Clues on Nebular Processes. *Meteoritics & Planetary Science* 38: 1399–1418.

Weidenschilling, S. J. 1977. Aerodynamics of Solid Bodies in the Solar Nebula. *Royal Astronomical Society*. *Monthly Notices* 180: 57–70.

Yang, L., and Ciesla, F. J. 2012. The Effects of Disk Building on the Distribution of Refractory Materials in the Solar Nebula. *Meteoritics & Planetary Science* 47: 99–119.